DESIGN AND IMPLEMENTATION OF A PARABOLIC TROUGH COLLECTOR SYSTEM

by
Egemen Orhan Bilgin
B.S., Mechanical Engineering, Istanbul University, 2015

Submitted to the Institute for Graduate Studies in
Science and Engineering in partial fulfilment of
the requirements for the degree of
Master of Science

Graduate Program in Mechanical Engineering
Boğaziçi University
2019

ACKNOWLEDGMENTS

First of all, I would like to thank my thesis advisor Assoc. Prof. Hasan Bedir and co-advisor Prof. Günay Anlaş for their great support during my study and the establishment of my experimental setup. Their encouragement and knowledge allowed me to finish my research.

I would like to thank my BURET lab mates Alpay Asma and Mehdi Nabati for their great support, friendship and great memories. Also, I would like to thank Doğu Hazar Kenar, Umut Soysal, Mert Can Arslanoğlu, and Orçun Çelebi for their efforts, help, and friendship.

Finally, I am a lucky person to have such a family who always supported me without questioning anything, thanks to my father, mother, and sister. Also, thanks to my best friend Taylan Ataysagğın for his motivation and encouragement.

ABSTRACT

DESIGN AND IMPLEMENTATION OF A PARABOLIC TROUGH COLLECTOR SYSTEM

With the effect of global warming on weather, most countries are interested in renewable energy sources and solar energy is the most promising one among others with an endless source. With this awareness, a lab scale test setup with an existing parabolic trough solar collector was designed and implemented with the aim of measuring inlet and outlet temperatures from the collector to calculate the thermal efficiency, useful heat gain, heat loss, and optical efficiency. A boiler was used as thermal storage with its two coils inside. Also, a solar tracking system was put into practice to follow the movement of the Sun to decrease the angle of incidence. The experiments were performed at Boğaziçi University Renewable Energy Technologies Laboratory on Sarıtepe Campus. As a result of experiments, maximum temperature and maximum thermal efficiency are found to be 65.25°C at 3.20 P.M. and 14.5% at 3:30 P.M. Moreover, the transition and turbulent flow are observed in the receiver at around 60°C.

ÖZET

PARABOLİK OLUKLU GÜNEŞ KOLEKTÖRÜ SİSTEMİNİN TASARIMI VE UYGULANMASI

Küresel ısınmanın iklim üzerindeki etkisiyle birlikte çoğu ülke yenilenebilir enerji kaynaklarıyla ilgilenmekte ve güneş enerjisi sonsuz kaynağıyla bu enerji kaynaklar arasında en umut verici olanıdır. Bu farkındalıkla, giriş ve çıkış sıcaklıklarını ölçmek, ısıl ve optik verimi, faydalı enerjiyi ve ısı kaybını hesaplamak amacıyla kampüste bulundan parabolik oluklu güneş kolektörü için laboratuvar ölçeğinde bir sistem tasarlandı ve kuruldu. Sistemde çift serpantinli boyler ısı deposu olarak kullanıldı. Ayrıca güneşin aynalara geliş açısını azaltmak ve günlük hareketini takip etmek için güneş takip sistemi kullanıldı. Deneyler Boğaziçi Üniversitesi'nin Sarıtepe Kampüsü'ndeki Boğaziçi Üniversitesi Yenilenebilir Enerji Teknolojileri Laboratuvarında gerçekleştirildi. Deneyler sonucunda maksimum sıcaklık saat 14:20 de 65.25°C ve maksimum verim saat 15:30 da %14.5 olarak bulundu. Ayrıca sıcaklık 60°C civarında iken alıcı tüpte geçiş akışı ve türbülanslı akış gözlemlendi.

TABLE OF CONTENTS

LIST OF FIGURES

LIST OF SYMBOLS

A	Area, m^2
a	Accommodation coefficient
amb	(subscript) ambient
ann	(subscript) annulus gas
b	Interaction coefficient
C	Concentration ratio
c	Specific heat, kj/kgK
c	(subscript) collector
cond	(subscript) conduction
conv	(subscript) convection
D	Diameter, m
eff	(subscript) effective
f	Friction coefficient / Focal distance of collector, m
F'	Efficiency factor
F_R	Heat removal factor
g	Gravitational constant, m/s^2
g	(subscript) glass cover
G_b	Direct beam radiation, W/m^2
gi	(subscript) inner of glass cover
go	(subscript) outer of glass cover
h	Heat transfer coefficient, W/m^2K
htf	(subscript) heat transfer fluid
K	Incident angle modifier, rad
k	Thermal conductivity, W/mK
L	Length of collector, m
m	(subscript) mirror
max	(subscript) maximum
Nu	Nusselt number
op	(subscript) optical

p	Pressure, Pa
Pr	Prandtl number
r	(subscript) receiver tube
Ra	Rayleigh number
rad	(subscript) radiation
Re	Reynolds number
ri	(subscript) inner of receiver tube
r_m	Mirror radius, m
ro	(subscript) outer of receiver tube
S	Arc length of collector, m
std	(subscript) standard temperature
T	Temperature, K
th	(subscript) thermal
U_L	Overall heat loss coefficient
V	Velocity, m/s
vac	(subscript) vacuum
W	Width of collector, m
X_{end}	End losses

α	Absorptivity
β	Volumetric thermal expansion coefficient, 1/K
γ	Intercept factor
δ	Solar declination
ε	Emissivity
η	Efficiency
θ	Incidence angle, rad
θ_z	Zenith angle, rad
λ	Mean-free path, m
μ	Dynamic viscosity, kg/ms
ν	Kinematic viscosity m^2/s
ξ	Roughness, m
ρ	Reflectivity / density, kg/m^3
σ	Stefan Boltzmann constant, W/m^2K^4

τ	Transmissivity
φ_m	Half acceptance angle, rad
ϕ_r	Rim angle, rad
ω	Hour angle, rad

LIST OF ABBREVIETIONS AND ACRONYMS

AC	Alternative Current
ASHRAE	American Society of Heating, Refrigerating and Air-Conditioning Engineers
BURET	Boğaziçi University Renewable Energy Technologies
CSP	Concentrated Solar Power
DNI	Direct Normal Radiation
GF	Geometric Factor
HTF	Heat Transfer Fluid
IEA	International Energy Agency
IRENA	International Renewable Energy Agency
NASA	National Aeronautics and Space Administration
NREL	National Renewable Energy Laboratory
ORC	Organic Rankine Cycle
P&ID	Piping and Instrumentation Diagram
PLC	Programmable Logic Controller
PPI	Pores Per Inch
PTC	Parabolic Trough Collector
PTCs	Parabolic Trough Collectors
PV	Photovoltaic
R&D	Research and Development
SCE	Southern California Edison
SEGS	Solar Electric Generating System
TES	Thermal Energy Storage
US	United States
USA	United States of America
VFD	Variable Frequency Drive

1. INTRODUCTION

With the increasing population the human being is always in search for new energy sources to meet his demands. The world reserves various energy traditional sources such as coal, petroleum, hydro-power. Governments around the world have agreed that the lifetime of fossil fuels will expire in the foreseeable future and one cannot depend on them only with the growth of world population. In addition to the deficiency of fossil fuels, the energy collection and production methods from these fuels are demonstrated to affect the environment. Power generation from these fossil fuels affects humanity negatively: the air is polluted and there is global warming. In order to prevent environmental pollution, some alternative sources have been proposed such as solar, biomass, wind, geothermal, hydropower, and tidal energy. These energy sources are clean and reasonable. Therefore, most countries work on these renewable energy sources, and solar energy seems to be the most promising one among others with an endless source.

Solar radiation is the key factor for solar applications, and it is the radiation emitted simultaneously in all directions by the Sun. The amount of solar radiation received by any location on the Earth can be calculated using various formulations that are related to the geographic location (latitude and longitude), to the time of the day, and to the angles between the Sun and the Earth. The solar radiation data are available on governmental and private websites such as YEGM, NREL, Solargis, and NASA. Turkey has a great potential in terms of solar radiation, especially in the south region. The map of solar radiation in Turkey is given in Figure 1.1. According to the map, the yearly average global horizontal radiation varies between 1000 kWh/m² and 2000 kWh/m² in different regions of Turkey [1, 2]. At BURET on Sarıtepe Campus (N 41° 14' 38", E 29° 00' 47") where the experiments were conducted, the average global horizontal irradiation energy is 1434 kWh/m² [1, 3]. The designated location is suitable for low and medium temperature solar applications.

In spite of this huge solar radiation potential of Turkey, there is only one concentrated solar power plant in operation, which is Greenway Solar Tower in Mersin. It was constructed in 2013 with a net turbine capacity of 1 MW. The power plant uses Rankine Cycle to generate electricity and has a single 3-phase molten salt thermal storage with a capacity of 4 MW [4].

Figure 1.1. Yearly average solar radiation map of Turkey [1].

Mainly two different technologies are used to generate power with solar energy: photovoltaic (PV) involving concentrated PV (CPV) and the flat-plate PV, and concentrated solar power (CSP). The former one immediately turns sunlight into electric using the photovoltaic cells. The latter one firstly concentrates the solar energy onto a line or point, then converts it into heat to produce power through a power cycle. A brief comparison is shown in Table 1.1.

Table 1.1. Comparison of PV and CSP [3, 4].

	PROS	CONS
PV	Low capital investment Low maintenance cost High efficiency	Produces less energy Economic returns in long term Small energy storage systems
CSP	Produces more energy Economic returns in short term Large energy storage systems	High capital investment High maintenance cost Low efficiency

Nowadays, photovoltaics have been used and are considerably popular; CSP technologies have also been developing rapidly. By 2030, 261 GW installed capacity of CSP, and 1721 GW installed capacity of PV will be achieved globally according to the forecast by the International Energy Agency (IEA) [7].

In 2016, 110 MW CSP capacity came online, and global capacity exceeded 4.8 GW at the end of the year. It was the lowest yearly growth rate with 2% in the total world capacity of 10 years [8].

CSP is the very first candidate to provide required renewable energy since it is among the most cost-effective renewable technologies. The working principle of CSP technologies is based on the concentration of sunlight to a certain point or line by using different mirror configurations. It is the most effective way of increasing the heat transfer fluid (HTF) temperature circulating in the system. A receiver collects this solar energy and converts into heat to obtain steam for a power cycle to generate electricity. This heat can be used for industrial processes or domestic applications such as heating or cooling. The total installed capacity of CSP technologies was 5496 MW worldwide according to capacity statistics of IRENA at the end of 2018 [9]. Currently, this capacity has increased to 6278 MW worldwide [4].

There are mainly four different CSP configurations:

- Solar Tower
- Linear Fresnel
- Parabolic Dish
- Parabolic Trough

Solar tower or central receiver displayed in Figure 1.2 is surrounded with two-axis sun-tracking mirrors (heliostats) on the ground, and these mirrors reflect solar irradiation onto a point receiver at the top of the tower which is high up to 100-200 m. They achieve high concentration ratio in the range of 300-1500, therefore are so effective in collecting energy and generating electricity [10]. The maximum operating temperature is in the range of 250-800 °C depending on HTF [11]. Currently, solar tower projects constitute almost 23% of CSP projects worldwide [4].

Figure 1.2. Solar tower [12].

Linear Fresnel systems as shown in Figure 1.3 consist of flat or slightly curved mirrors that rotate in single axis on the ground level. Mirrors reflect sunlight into a fixed line absorber located several meters above mirrors. Fresnel mirrors have an advantage in their price due to its shape compared to PTC. Presently, approximately 3% of the CSP systems are Fresnel systems worldwide [4].

Figure 1.3. Linear fresnel [13].

Parabolic Dish systems as in Figure 1.4 consist of a reflector shaped like a dish and a point receiver which can rotate in two-axis with the concentration ratio between 600-2000 [10]. Because parabolic dish systems always focus the sunlight, they are identified as the most efficient among CSP systems [10]. The receiver is positioned at the central point of the parabolic dish. Also, each parabolic dish has its engine (generally Stirling engine) mostly located at the receiver to convert heat energy into electricity. Despite its high efficiency, it is not favorable among others due to high cost of the Stirling engine.

Figure 1.4. Parabolic dish [14].

Parabolic trough systems illustrated in Figure 1.5 are the most mature systems among the CSP configurations. Currently, the majority of solar thermal power plants use PTC systems. [15].

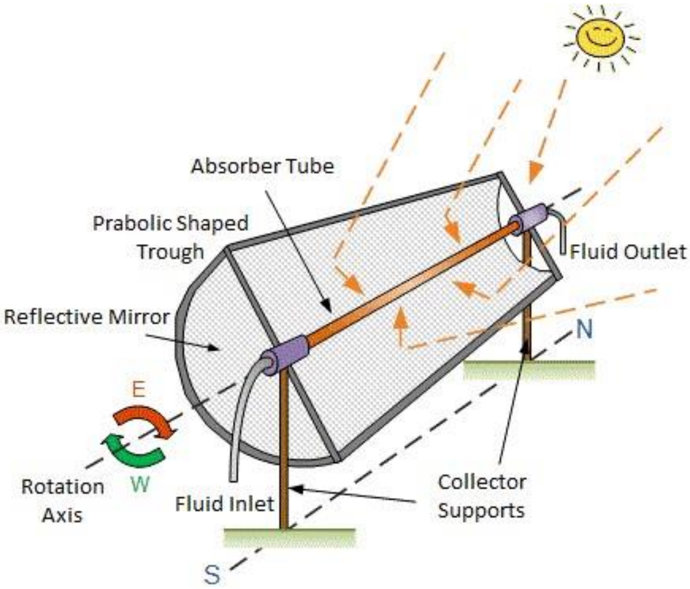

Figure 1.5. Parabolic trough [16].

Parabolic trough systems consist of a supporting structure, reflective mirrors, a tracking system, and an absorber tube placed on the focal lines of parabolic collectors. The piping instrument of the absorber tube is made from different materials such as steel, metal or plastic and mostly covered by a glass envelope. Vacuuming the air in between the glass envelope and absorber tube decrease convective heat losses and allow thermal expansion. It is also essential that a glass-to-metal seal decreases the heat losses as well. The metal tube is coated with a particular material such as black chrome or cermet which has high absorbance [15].

Majority of the parabolic trough power plants heat oil then thermal energy is conveyed to water from the oil through heat exchangers. In order to drive the steam turbine, water changes the phase to superheated steam. Then, the cooled oil recirculates through the PTC for reheating. There are a few studies that directly produce superheated steam through PTC without a heat exchanger [17] such as [18]. PTCs only concentrate the direct beam radiation with the concentration ratio of 70-80 [19]. Existing PTCs can heat the HTF to 400°C. The tracking systems are usually utilized to rotate about the north-south axis that optimizing the yearly generated power. On the other hand, rotation on the east-west axis can optimize the power generation in winter [20].

At the beginning of the 1970s, research and development of CSP plants and PTC technology increased as a result of the oil crisis. SEGS (Solar Electric Generating System) projects have been demonstrated as a way of producing electricity, and nine PTC power plants were constructed in Mojave Desert, California. Their capacities were in the range of 14 to 80 MW with a total capacity of 354 MW [4].

The first recognized PTC was built by Swedish John Ericsson in 1880 [20]. It was used to operate a hot air engine. The first patent of PTC was taken out by Adolf Remshardt and Wilhelm Meier in 1907 [20]. The aim was to produce water. In 1913, a 45-kW pumping plant for irrigation was constructed by British Frank Shuman and Charles Vernon Boys in Maadi, Egypt, using PTCs. Steam engines, which received the steam from the PTCs, have actuated the pumps. They used PTCs with 1200 m² total aperture area, with a length of 62 m and width of 4 m. The system was able to pump twenty-seven thousand liters of water per minute. The plant was successful; however, it was closed in 1915 with the outbreak of World

War I and with low fuel costs the application of combustion technologies more profitable [19, 20].

The popularity of PTC technology rose after 1977 when the Ministry of Research and Technology of Germany and the US Department of Energy started to fund the progress of various water pump systems and heat machines using PTCs. Governments needed to encourage the usage of PTC because of high fossil fuel prices. Some of the results of these precautions are listed below [20]:

- PTC display system with nearly 10,000 m² total aperture area was built by Acurex company in the USA to process heat operations between 1977 and 1982 [20].
- In 1979, the first modern line focusing CSP plant was constructed in Coolidge, Arizona with a capacity of 150 kWe [22].
- The building display facilities project with a capacity of 500 kW was put into operation in 1981 at the Plataforma Solar de Almeria with the participation of nine member states of the IEA [20].
- The first process heat machine funded privately with an aperture area of 5580 m² PTCs was successfully started to operate in 1983 in Arizona with the aim of thermal heating for electrolyte tanks in a copper processing firm. These systems improved to obtain temperatures higher than 260°C for industrial process heat implementations [20].

In 1983, an agreement was signed with Luz International Limited by Southern California Edison (SCE) to buy energy from the first two commercial solar power plants built in the Mojave Desert in California. These power plants, named SEGS I and II, were put in operation in 1985 and 1986 respectively. Later, with the agreement of these two companies, SEGS III to SEGS IX power plants were constructed. In the beginning, the plant size has a limitation of 30 MW, but then it increased to 80 MW. The installed capacity of these nine power plants was 354 MW [14, 20].

Andasol I is the very first commercial PT power plant in Europe. It is producing power since December 2008 in the Granada, Spain. In 2009 and 2011 constructions of Andasol II and III was finished and they are connected to the grid. The capacity of each power plants is 50 MW. These three power plants were the first projects with large thermal storages with a capacity of 28,500 tons of molten salt for 7.5 hours peak load [6, 16].

Thus far, a brief and comparative information are mentioned about CSP technologies and PTC with the historical improvements. Many researchers have focused on to maintain developments in the area, including modeling, design and implementing, and performance assessments. A literature review is given in the next section to better understand and determine the existing problems having been faced in the design, manufacturing and performance evaluation.

1.1. Literature Review

In the literature, many experimental studies are conducted with parabolic trough collectors and relevant ones are mentioned below:

Mohamed Chafie *et al*. [24] designed and manufactured a PTC system with 10.8 m^2 aperture area under Tunisian climate and published an experimental study. The purpose was to evaluate the thermal performance, and to do that some parameters were measured such as the thermal efficiency, the incident angle modifier, and the heating and cooling time constants. The peak thermal efficiency was obtained to be 55.1%. Moreover, various conditions such as the ambient temperature and solar radiation were investigated in the study. Experiments were conducted on typical days, sunny and cloudy day. As a result of experiments, for sunny and cloudy days, a mean thermal efficiency was obtained to be 41.09% and 28.91%. Also, the mean useful heat gain was 252.59 W/m^2 and 171.52 W/m^2 when the time constant were 137s and 220s respectively.

Rehan *et al*. [25] conducted an experimental performance assessment of a PTC with a low concentration ratio of 11 for non-commercial heating applications in Taxila, Pakistan. Water based nanofluids of Al_2O_3 and Fe_2O_3 were used as HTF with 0.2%, 0.25% and 0.3% particle concentration. Experiments were performed in winter for 2 months and flow rates were determined to be 1 1.5 and 2.5 liter per minute. As a result, water based nanofluids, Al_2O_3 and Fe_2O_3 were found to be 13% and 11% more efficient than using only water HTF at 2 L/min flow rate.

Potenza *et al.* [26] did experiments with a parabolic trough collector with 4 m^2 aperture area using gas-phase nanofluid. The absorber tube used in the experiments was transparent. This work aimed to explore the innovative issues identified with the usage of gas-based nanofluid combined with transparent quartz receiver. Experimental results showed a significant problem in the receiver tube related to nano powder deposition because of humidity. They saw a clear relationship linking dirtying and moisture of the nanofluid. Also, the evaluation of thermal performance demonstrated that the maximum HTF temperature was 180°C with 65% mean optical efficiency.

Wanjun Qu *et al.* [27] carried out tests on a 300 kW prototype PTC with a rotatable solar tracing system. With the rotation of the system, azimuthal angle, solar incidence angle, and cosine loss changed. In order to increase optical efficiency, the rotatable axis was used in winter, and the north-south axis tracing was used in summer. The mean daily efficiencies were measured as 63% and 40% in summer and winter respectively. Moreover, experiments were performed to compare the cosine effect in the winter. Results showed that the cosine loss decreased by 10.3% with the rotatable axis tracing. Thus, the mean daily efficiency was enhanced by 5% when it compared to north-south axis tracing.

Asfar *et al.* [28] designed a six-meter-long PTC in Jordan to evaluate its thermal performance. The aperture width, the rim angle and the concentration ratio were 1,67 m, 100º and 21 respectively. The maximum thermal efficiency reached in the experiments was 22.4%. At such a low flow rate of 2,67 l/h with a fixed inlet temperature of 27 ºC, the steam generated was 123ºC at pressure of 2 bars.

Filho *et al.* [29] conducted an experimental and analytical research on thermal losses of a 3m wide and 4m long parabolic trough collector with a vacuumed receiver tube with selective coatings to evaluate the global heat loss coefficient (heat flux divided by the area of the absorber tube and temperature difference). Heat loss measurements were performed under steady-state conditions. As a result of experiments, the global heat loss coefficient was found to be in the range of 4.49-6.93 W/m^2K with an average of 5.68 W/m^2K with an uncertainty of 45%.

Jamal-Abad *et al.* [30] carried an experimental studyon a PTC with a receiver pipe filled with copper foam to enhance efficiency and heat transfer. The density and porosity of the copper foam were 30 PPI (pores per inch) and 0.9 respectively. Experimental tests were conducted with flow rates between 0.5 and 1.5 L/min and ASHRAE 93 standards [31] were used to evaluate the results. Experiments showed that when the mass flow rate increased, the collector's efficiency improved. The same behavior in the system was observed when the receiver tube was filled with copper foam because of a 45 % decrease in the overall loss coefficient.

Another experimental study of PTC for industrial process heat was conducted by Coccia *et al.* [32] with a 90° rim angle and 9.25 low concentration ratio. The tests were conducted in Ancona, Italy using ASHRAE Standard 93 as a reference and demineralized water was used as an HTF with 300 L storage tank. The flow rate was determined as 0.045 kg/s just a little above the reference flow rate (0.037 kg/s). As a result, the slope was found to be -0.683 from the thermal efficiency equation which can be related to thermal losses, and the intercept value was 0.658 as an indicator of the optical performance.

Zou *et al.* [33] investigated a small-sized PTC that introduced to heat water in cold regions. It was manufactured in small-size to get rid of the shortcomings of traditional solar collectors such as low efficiency, freezing, tube-burst, and significant heat loss, which restrict their practical application due to cold weather. Experiments were performed to measure the characteristics of their PTC. There were three parts to the study: thermal efficiency analysis, anti-freezing analysis, and the comparison test between the coated group and uncoated one. The results showed a peak thermal efficiency of approximately 67% although solar radiation was about 310 W/m^2 if the emissivity of mirrors were very high. Furthermore, when the water temperature was under 100°C, because of the increase in Reynolds number stimulated by the thermophysical parameters of the HTF, the thermal efficiency enhanced with rising water temperature. Under freezing and 5.0 m/s wind velocity conditions, peak thermal efficiencies were 26% and 56% respectively. Moreover, they compared the coated absorber with the uncoated one and result demonstrated that coated double-glazing absorber produced more extensive temperature response delay to the deflected sunray. The PTC showed a great anti-freezing feature in a cold environment at low HTF temperatures.

Qu *et al*. [34] studied experimental by a medium temperature parabolic trough solar thermal system. They designed and manufactured a PTC with an 84° rim angle, 4.2 m length, and 6.72 m² aperture area in Yantai, China, where radiation source is medium. In order to provide a rotation in north-to-south direction, a PLC solar tracking system was used. PTC's thermal performance was evaluated under a variety of weather and working conditions according to national and global standards. The results showed that the cosine effect, end loss, incident angle modifier, and effective radiation, which are optical effects involving the shade effect, are worth paying attention. The experiment demonstrated that the peak efficiency was 72%.

Lei *et al*. [35] characterized thermal properties of a 50 MW PTC in Inner Mongolia, China. They examined end loss, overall heat loss, and coating thermal emittance of a new composed absorber tube. By using the steady-state equilibrium method, which converts electrical power to heat under steady-state conditions, heat loss experiments were performed. A correlation was obtained between the heat loss and the temperature of the receiver. In order to overcome the problems and testing the coating emittance more accurately, a new examination method was presented. This method was evaluated to keep high vacuum and continuous exhaust along with the heat loss examining with the help of a robust vacuum gauge and a vacuum system. Comparing these heat loss measurements with other commercial receivers allowed further optimization as a reference. In experiments, two Himin PTR-2011 receivers were used. As a result, rising the temperature of the receiver tube caused a rapid increase in heat loss. The heat losses were 110, 180 and 270 W/m at the mean absorber tube temperatures of 300, 350 and 400 °C respectively. With these values, a relation was evaluated between the temperature of the receiver and the heat loss to calculate the heat loss at different temperatures. Himin PTR-2011 demonstrated exceptional thermal performance and reduced heat loss in PTC when it was compared to other receivers such as Schott 2008 PTR-70 and Solel UVAC3.

Sivaram *et al*. [36] performed experimental and numerical investigations of a solar PTC with 7.5 m² aperture area combined with a 60 L thermal energy storage unit. Water and paraffin were used as HTF and phase change material respectively; paraffin behaves like a reasonable energy storage medium. The impact of flow rate on useful heat gain, stored energy, and thermal efficiency, was studied. To find out temperature distribution, thermal losses, and heat fluxes, a numerical method was proposed for the absorber element based upon one-dim heat transfer equations. Experimental data were compared to the performance parameters obtained from the numerical method, and ten percentage difference was determined. The reason behind that difference was thought to be due to the fluctuation of incident solar radiation that used as input for the mathematical model. Three main reasons for the thermal loss were concentrated solar radiation, heat gained by HTF, and absorber tube temperature. There is higher heat loss (85%) between the absorber tube and glass cover because of the pressure of air. In the noon, maximum charging and overall efficiency were obtained to be 62.5% and 30% respectively and then the values declined due to a decrease in incident solar radiation.

Bortolato *et al*. [37] investigated a PTC with a flat bar-and-plate absorber tube for direct steam generation. Absorber tube with the bar-and-plate technology was produced and, it had an inner offset strip turbulator within the tube. It was supported with an asymmetrical PTC in order to create a collector with a concentration ratio of 42 that have examined experimentally. In order to evaluate the thermal performance of the PTC throughout steam generation, a new test method was introduced, practiced and validated. The results demonstrated that the overall thermal efficiency was found to be 64%.

Lu *et al*. [38] investigated a solar PTC and evaluated a heat loss analysis. The heat loss of the solar PTC with 10.2 m length and 0.12 m diameter was measured experimentally. The main reasons behind the heat loss of the absorber tube were the heat loss from the glass and boundary region, and generally, it reduces by the temperature of the tube wall. As a result of the analysis, the heat loss of the absorber tube, glass, and boundary sections are 987.1 W, 762.2 W, and 224.9 W respectively when the temperature of the absorber wall and circumference are 176.2°C and 31.0°C respectively. The minimum heat loss could be reached under some specific temperature of wind and wall conditions. The heat transfer within the glass envelope mostly relied on radiation, while the natural convection and radiation outside of it had a significant role. Experimental results were in a good agreement with the calculations of heat loss due to the convection at the surface of the glass and radiation within the glass.

Kumaresan *et al.* [39] performed an experimental and analytical study of thermal performance improvement in absorber tubes of solar PTCs. Experimental and numerical works were performed to enhance heat transfer concentrate upon minimizing of the heat loss, the use of turbulators, nanofluid, and selective coatings in the absorber tube. The main reasons behind the heat loss in the absorber were inaccurate vacuuming between the glass cover and the absorber tube, end losses in the absorber, coating degradation at high temperatures, distribution of temperature in the absorber, hydrogen accumulation and diffusion in the absorber tube, and cracking of fasteners at the edges of the absorber tube. The advantage of using nanofluids as HTF was an increase in the solar absorption intensity and heat transfer in the absorber tube.

Soysal U. [40] analyzed and optimized a small-scale solar Organic Rankine Cycle system to generate power. In order to evaluate the annual performance of this small-scale system under the climate of Istanbul, a numerical model was developed. The thermal model of the PTC was developed and the generated heat was compared to experimental data. The ORC system, which is consisted of an evaporator, a condenser, a pump, and an expander, was used for the power block. R245fa was used in the system as a working fluid, and the system was developed in MATLAB. Optimization studies on mass flow rates, collector aperture area, and pressures were performed. The efficiency of the system was 6.4% with 96.72 kWh produced energy, without thermal storage. With the implementation of 4 m^3 thermal storage, the overall efficiency increases to 7.18% and total produced energy are 108 kWh.

Çağlar A. [41] designed a PTC using a high reflectivity concentrator. To enhance the optical efficiency, he used two different reflective surfaces and compared them: 316-L chrome plate and aluminum composite panel. Experiments were conducted in Antalya, Turkey; the measured the temperature inside the storage (20 L). There were three different cases in experiments: 316-L chrome plate with a glass cover, 316-L chrome plate without a glass cover, and aluminum composite panel without a glass cover. Efficiencies were found to be 0.92, 0.73 and 0.82 respectively. These results show that aluminum composite has a better performance as reflectance and the glass cover is significant for optical efficiency.

Murtuza *et al.* [42] studied a 5 m long PTC experimentally and numerically. Experiments were performed on a yearly scale in Ramanagaram, India at various flow rates: 0.4 L/m, 0.8 L/m and 1.2 L/m. The Reynolds number was calculated for each flow rates. In between the March and May, a high outlet temperature range was observed between 93°C-103°C. Thermal efficiencies were given with increasing Reynolds number. Results showed that the thermal efficiency reduced with increasing Reynolds number.

Kumar D. and Kumar S. [43] performed an experimental research to evaluate the thermal performance of a PTC at different flow rates. A PTC was designed with 90° rim angle, 1.33 m^2 aperture area, and water was used as the HTF. They carried out experiments at six different mass flow rates: 0.001, 0.002, 0.005, 0.01, 0.02, and 0.024 kg/s with glazing and without glazing heat collectors. As a result of experiments, the maximum HTF outlet temperature was found to be 54.7°C, and the peak efficiency was 53.33%.

In summary, there are several experimental studies published to evaluate the performance of PTC in literature. Majority of these studies aim to observe the effects of the parameters such as flow rate and heat transfer fluid on heat loss and thermal and optical efficiency. It is observed that the thermal efficiency is enhanced with the increasing mass flow rate if the flow is laminar. However, Murtuza *et al.* [42] showed the exact opposite; the thermal efficiency is decreased with the increasing Reynolds number when the flow is turbulent. Therefore, the turbulent flow case in the absorber tube is significant to investigate. Moreover, enhancements in heat transfer mechanism with the usage of nanofluids as an HTF are proven in many studies. Furthermore, the effects of the glass cover, vacuuming, and coating to overcome the heat losses are demonstrated with comparative experimental studies. Most non-commercial PTC prototypes have a concentration ratio in the range of 30 to 100 and there are only few studies to investigate the effects of low concentration ratio ($C<20$). Also, most non-commercial PTC prototypes in experimental studies have smaller aperture areas (1-12 m^2) than utilized PTC (15 m^2) in this thesis.

With this knowledge, a PTC test setup with a low concentration ratio will be designed to investigate the transition and turbulent flow in the system. The instrumentation of lab scale setup will be selected to provide turbulent conditions in the system. Also, a boiler will be implemented as a thermal storage distinctly from the literature.

1.2. Objectives

The main objectives of the proposed study are as follows:

- Experimental investigation of PTC having low concentration ratio using thermal oil as an HTF to evaluate thermal and optical efficiency, heat loss, and heat gain
- Investigating the consequences of turbulent flow in the system over the thermal efficiency and heat loss
- Obtaining hot water at a constant temperature for the medium temperature applications such as Organic Rankine Cycle
- Increasing the awareness level of CSP technologies in my Turkey since there is only one commercial solar power plant despite the great solar potential.

In this study, an experimental setup will be designed for PTC with low concentration ratio for medium-temperature applications to evaluate heat losses and the optical and thermal efficiency. Tests will be performed at BURET, on Sarıtepe Campus, Istanbul where the yearly average direct normal irradiation is 1258 kWh/m^2 per hour. A solar tracking system will be used to increase the optical efficiency. A data acquisition system will be applied to obtain experimental data such as inlet and outlet temperature of the receiver, the mass flow rate, and temperature of the tank. According to data of experiments, the thermal and optical efficiency, heat gain and heat losses will be calculated.

2. BACKGROUND

2.1. Solar Radiation

In this section some fundamental definitions of solar radiation are given to understand relations better between the Sun and the Earth. The radius of the Sun (R_s) is 6.95×10^8 m and the surface temperature is considered to be 5777 K (T_{sun}) [44]. The average distance between the Earth and the Sun ($D_{e\text{-}s}$) is 1.491×10^{11} m. The solar constant, $I_{sc,}$ is the intensity of the solar radiation hitting on a unit area of a surface on the Earth and it is calculated as:

$$I_{sc} = \sigma T_{sun}{}^4 \left(\frac{R_s}{D_{e-s}}\right)^2 \tag{2.1}$$

The average value of the solar constant is 1372 W/m². That value is changed between 1336 W/m² and 1410 W/m² with the movement of the Earth and it is accepted as 1367 W/m² in literature.

2.1.1. Geometric Relationship of the Sun and the Earth

The Earth completes revolving around the Sun within 365 days. The Earth-Sun distance changes with the time due to the elliptical orbit of the Earth's movement. The distance between the Sun and the Earth is maximum on June 21 with a value of 1.512×10^{11} m (which is called aphelion), and minimum on December 21 with a value of 1.471×10^{11} m (which is called perihelion) [45]. The axis of the Earth's daily rotation around itself is at an angle of 23.45° to the axis of its ecliptic orbital plane around the sun (Figure 2.1). This tilt is the main reason for the seasonal change of the available solar radiation at any location on the earth. The angle between the Earth-Sun line (through their center) and the plane through the equator is called the solar declination angle, δ .The declination angle varies between -23.45° on December 21 to +23.45° on June 21. The solar declination is defined as [45]:

$$\delta = 23.45^\circ \sin\left(\frac{360}{365}(284 + n)\right) \qquad (2.2)$$

where n is the day of year ($1 \leq n \leq 365$). The change of solar declination is given in Figure 2.2.

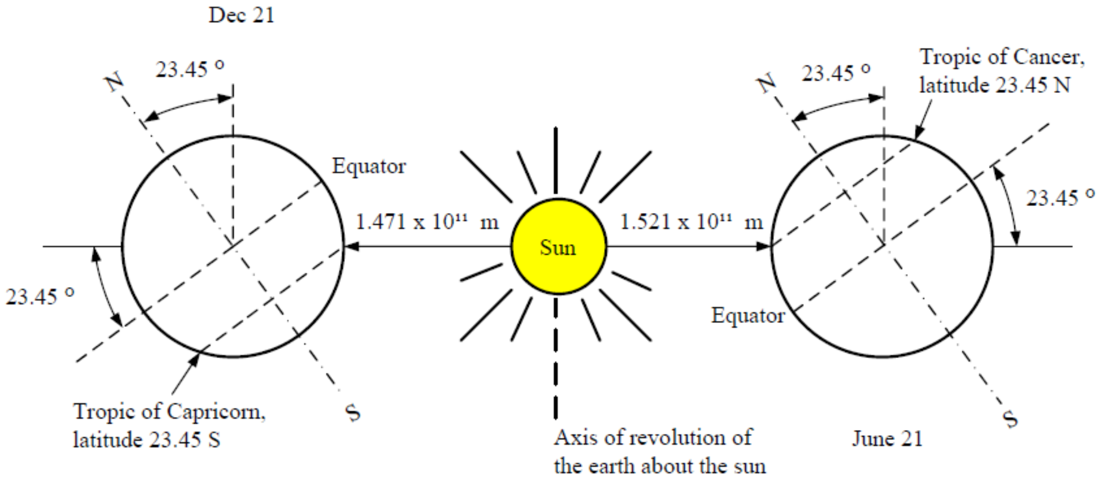

Figure 2.1. Motion of the Earth around the Sun [46].

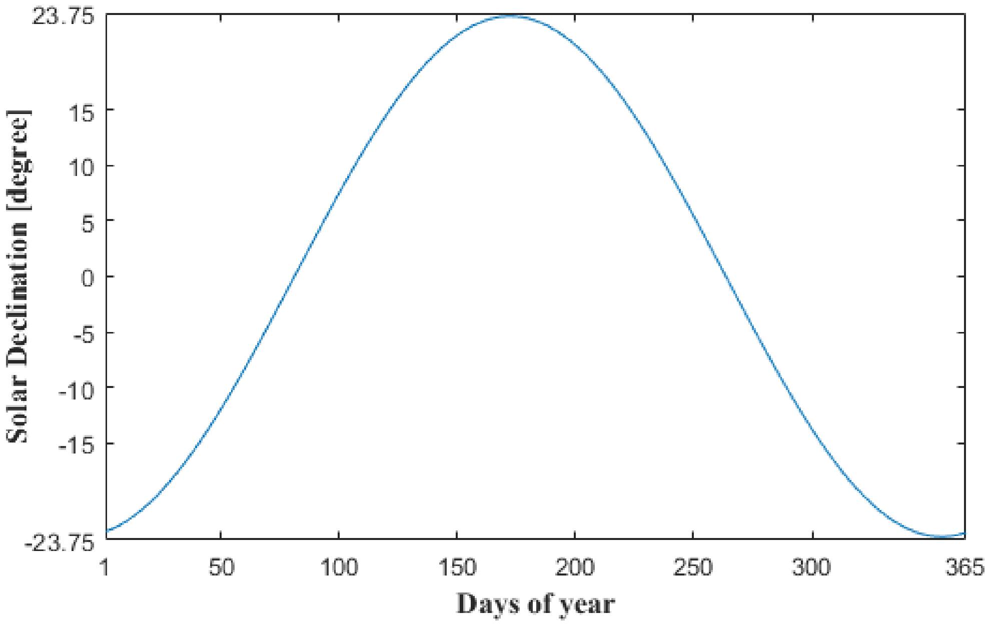

Figure 2.2. Solar declination variation throughout the year.

2.1.2. Extraterrestrial Radiation

Extraterrestrial radiation (I) can be defined as the amount of energy received per unit time on a unit area of a surface perpendicular to the Sun outside the atmosphere of the Earth. It is calculated as:

$$I = I_{sc}\left(1 + 0.033\cos\left(\frac{360}{365}n\right)\right) \tag{2.3}$$

where n is the day of year. Change of extraterrestrial with days of year is given in Figure 2.3.

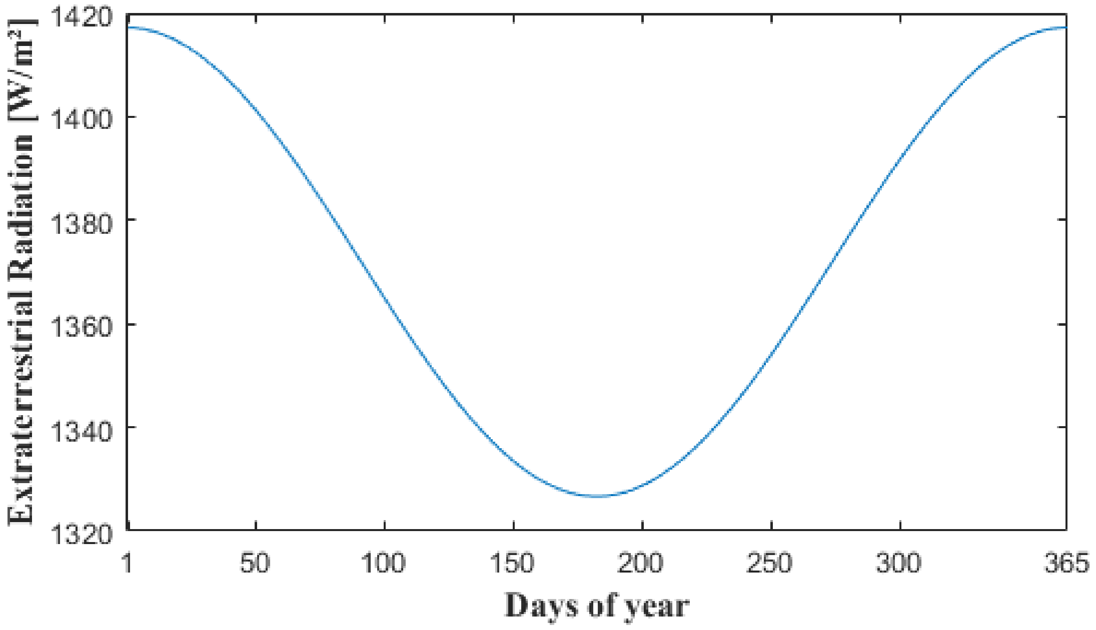

Figure 2.3. Variation of extraterrestrial throughout the year.

2.1.3. Terrestrial Radiation

Extraterrestrial solar radiation that passes through the atmosphere of the earth is reduced due to reflection, absorption and scattering as shown in Figure 2.4. The part of the energy that is directly received at the surface of the earth without being essentially scattered is called direct of beam radiation, I_b, and the amount of energy passing the atmosphere and reaching the earth's surface with being scattered considerably is known as sky diffuse radiation, I_d. The summation of beam radiation and sky diffuse radiation is called global horizontal radiation, I_H.

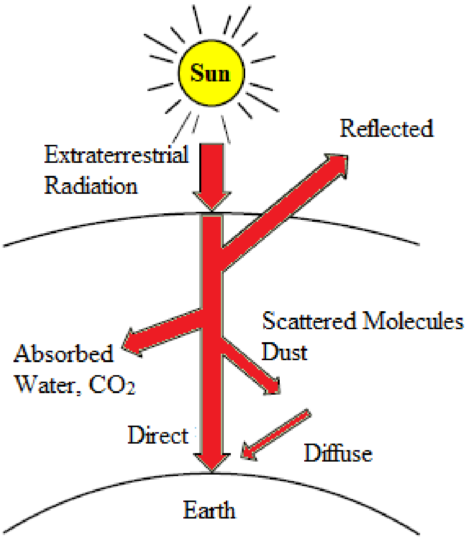

Figure 2.4. Attenuation of solar radiation as it passes through the atmosphere [46].

Correlation between these definitions as follows:

$$I_H = I_b + I_d \tag{2.4}$$

$$I_b = DNI\cos(\theta) \tag{2.5}$$

$$DNI = A \cdot \exp\left(-\frac{B}{\cos\theta}\right) \tag{2.6}$$

$$I_d = C \cdot DNI \tag{2.7}$$

where DNI is the direct normal radiation, A,B, and C are constants which vary throughout the year. There are models to estimate these constants; ASHRAE model is given in Figure 2.5.

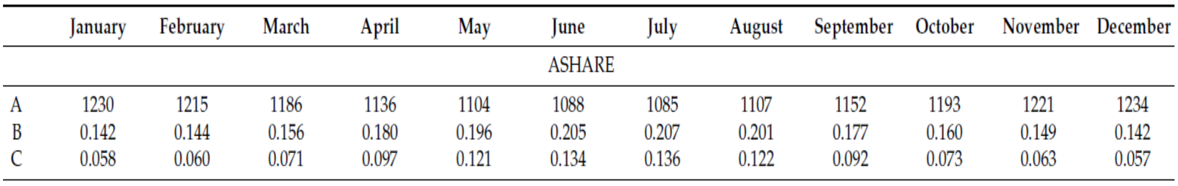

	January	February	March	April	May	June	July	August	September	October	November	December
						ASHARE						
A	1230	1215	1186	1136	1104	1088	1085	1107	1152	1193	1221	1234
B	0.142	0.144	0.156	0.180	0.196	0.205	0.207	0.201	0.177	0.160	0.149	0.142
C	0.058	0.060	0.071	0.097	0.121	0.134	0.136	0.122	0.092	0.073	0.063	0.057

Figure 2.5. ASHRAE model for A,B, and C constants [47].

2.2. Geometry and Parameters of Parabolic Collector

In this section, geometrical parameters of parabolic trough collectors are introduced for a better understanding of design parameters. First of all, law of reflection given in Figure 2.6 is the fundamental for the reflection of sunrays. The law of reflection states that the angle of reflection equals the angle of incidence: $\theta_i = \theta_r$.

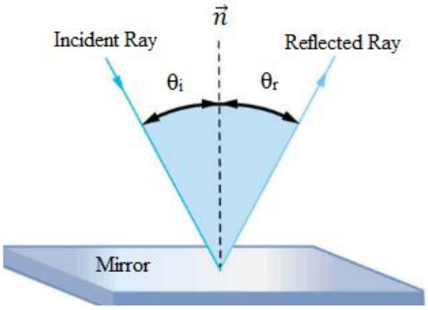

Figure 2.6. Law of reflection.

The shape of parabolic collectors is be defined with the parabola geometry as in Figure 2.7.

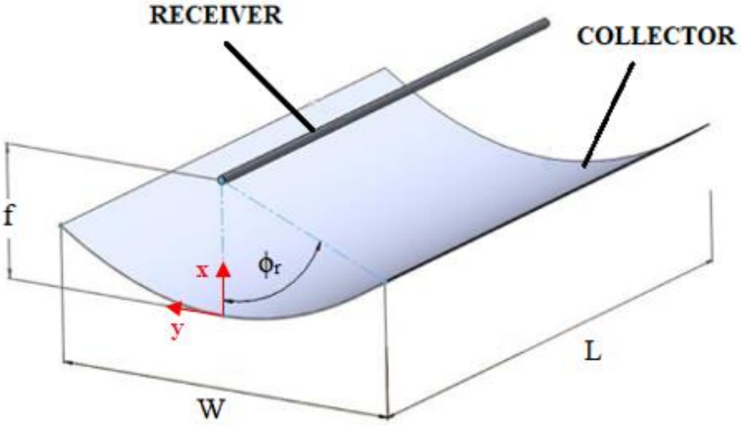

Figure 2.7. 3D geometry of parabola.

In this figure, ϕ_r is the rim angle, L is the length, W is width (aperture), and f is the focal distance of parabola. The formulation of the parabola is:

$$x = y^2/4f \tag{2.8}$$

The rim angle ϕ_r is defined with the following equations [20], where r_m is the radius of mirror. Also, a relation between the rim angle and W/f value is given below:

$$\phi_r = \tan^{-1}\left[\frac{8(W/f)}{16-(W/f)^2}\right] = \sin^{-1}\left(\frac{W}{2r_m}\right) \tag{2.9}$$

$$r_m = \frac{2f}{1+\cos\phi_r} \tag{2.10}$$

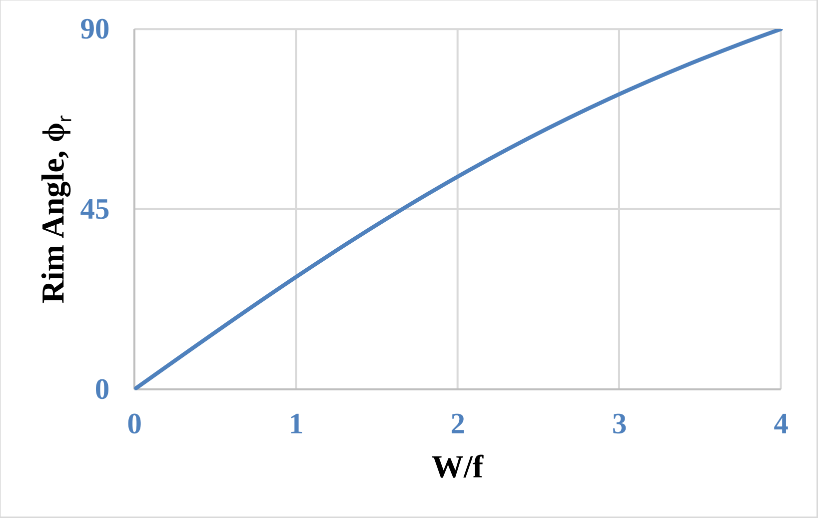

Figure 2.8. Relation of rim angle and W/f ratio.

The total aperture area of the collector A_c is introduced as [48]:

$$A_c = WL \tag{2.11}$$

Also, the receiver/absorber tube area A_r is given by:

$$A_r = \pi D_{ro} L \tag{2.12}$$

where D_{ro} is the outer diameter of the receiver. The half acceptance angle θ_m is another important parameter to define the minimum size of receiver outer diameter with the following equation:

$$D_{ro} = 2r_m \sin\varphi_m \tag{2.13}$$

With these definitions, the ratio of total aperture area of the collector A_c to the area of receiver/absorber A_r is represented as concentration ratio C; that is [19],

$$C = \frac{A_c}{A_r} \tag{2.14}$$

$$C = \frac{W}{\pi D_{ro}} \tag{2.15}$$

Substituting equations (2.9) and (2.13) into equation (2.15):

$$C = \frac{\sin \phi_r}{\pi \sin \varphi_m} \tag{2.16}$$

For an ideal case, with 90° rim angle ϕ_r and 0.267° half acceptance angle φ_m, the maximum concentration ratio is found to be 68.3 [49].

ϕ in Figure 2.9 is the angle between the collector axis and a reflected beam at the focus.

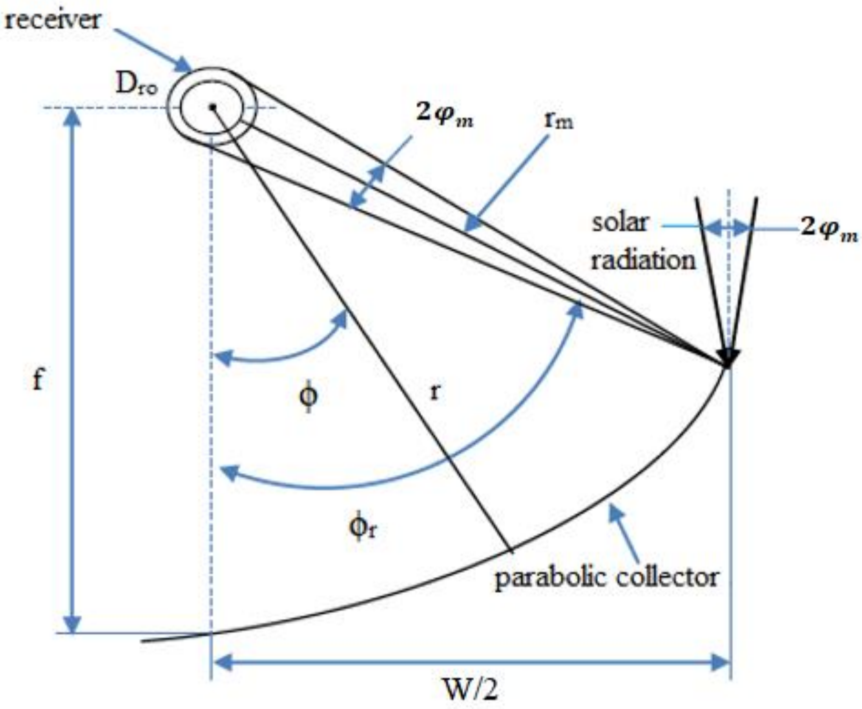

Figure 2.9. Cross section of the collector [19].

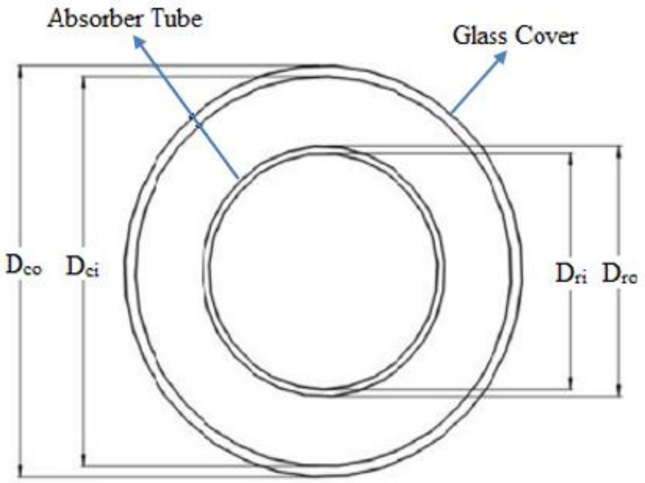

Figure 2.10. Cross section of the receiver.

The receiver consists of an absorber tube and a glass cover. The air between the glass cover and absorber tube is generally evacuated to reduce the heat losses. The parameters of existing parabolic trough collector are given in Table 2.1.

Table 2.1. Parameters of PTC.

Focal distance, f	93.75 cm
Rim angle, ϕ_r	77.32°
Half acceptance angle, φ_m	0.9°
Width, W	3 m
Length, L	5 m
Aperture area, A_c	15 m^2
Receiver area, A_r	0.759 m^2
Mirror area, A_m	16.47 m^2
Outer diameter of the receiver, D_{ro}	48.3 mm
Inner diameter of the receiver, D_{ri}	40.8 mm
Mirror curve, S	3.29 m
Radius of mirror, r_m	153.75 cm
Concentration ratio, C	19.77
Outer diameter of the glass cover, D_{go}	70 mm
Inner diameter of the glass cover, D_{gi}	60 mm

2.3. Optical Analysis

The optical analysis of PTC helps us to determine the amount of solar energy received by the absorber tube where HTF circulates. In order to carry out the optical analysis of PTC, some parameters such as incidence angle modifier, end losses, and interception factor should be defined and determined. The optical efficiency is defined in [19] as:

$$\eta_{op} = \rho\tau\alpha\gamma[(1 - GF\tan\theta)\cos\theta] \tag{2.17}$$

where GF is described as the ratio of the shaded area to the total aperture area of the collector. Another definition for the optical efficiency is given by Bellos and Tzivanidis [48]:

$$\eta_{op} = \eta_{op,max}K(\theta) \tag{2.18}$$

$$\eta_{op,max} = \rho\tau\alpha\gamma \tag{2.19}$$

where the incident angle modifier K(θ) is defined by Gaul and Rabl [50]:

$$K(\theta) = 1 - \frac{f}{L}\left(1 + \frac{W^2}{48f^2}\right)\tan\theta \tag{2.20}$$

The previous equation for the incident angle modifier K(θ) is estimated with end and cosine losses of PTC. For a collector rotates about the horizontal north-south axis with an east-west tracking mechanism, the cosine of the incident angle is computed with the following equation using some angles of sun:

$$\cos(\theta) = \sqrt{\cos^2(\theta_z) + \cos^2(\delta)\sin^2(\omega)} \tag{2.21}$$

Moreover, the incident angle modifier can be estimated with experimental results, with the optical efficiency definition in [51]:

$$\eta_{op} = \rho\tau\alpha\gamma K(\theta)X_{end} \tag{2.22}$$

2.3.1. Incident Angle Modifier

The angle between solar beams and the normal surface of a collector is represented as the angle of incidence (θ), and cosine of this angle affects the solar radiation. Therefore, the term incident angle modifier (K(θ)) is specified to adjust the cosine effect of angle of incidence. The incident angle modifier is represented as the proportion of the optical efficiency in certain incident angle to maximize optical efficiency where the θ=0°, as shown in the following equation:

$$K(\theta) = \frac{\eta_{op}(\theta > 0°)}{\eta_{op,max}(\theta = 0°)} \tag{2.23}$$

For a collector plane tilted with an α angle is shown in Figure 2.11.

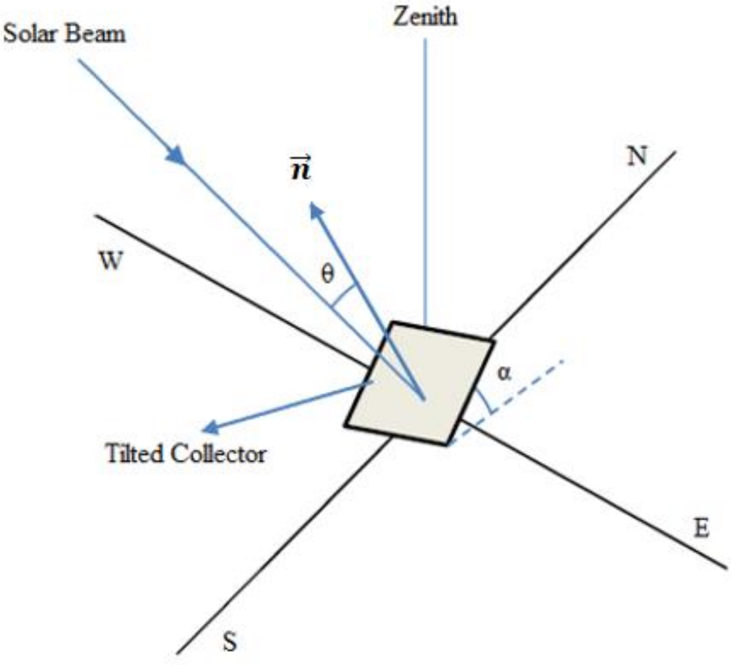

Figure 2.11. Angle of incidence.

Also, the incident angle modifier can be estimated with the experimental data as a polynomial equation. The change of incident angle modifier with the angle of incidence is shown in Figure 2.12. After the 77° of incident angle, solar beams cannot reach to the receiver of PTC. 40° seems like an attractive point to mention since the incident angle modifier is 0.8 and the optical efficiency is acceptable in the range of 0-40 degrees [52]. Therefore, the implementation of a solar tracking system is significant to adjust the incidence angle in this range. The polynomial estimation of the incident angle modifier with the change of incident angle is found as:

$$K(\theta) = -4 \times 10^{-6}\theta^3 + 0{,}0003\theta^2 - 0{,}0114\theta + 1 \tag{2.24}$$

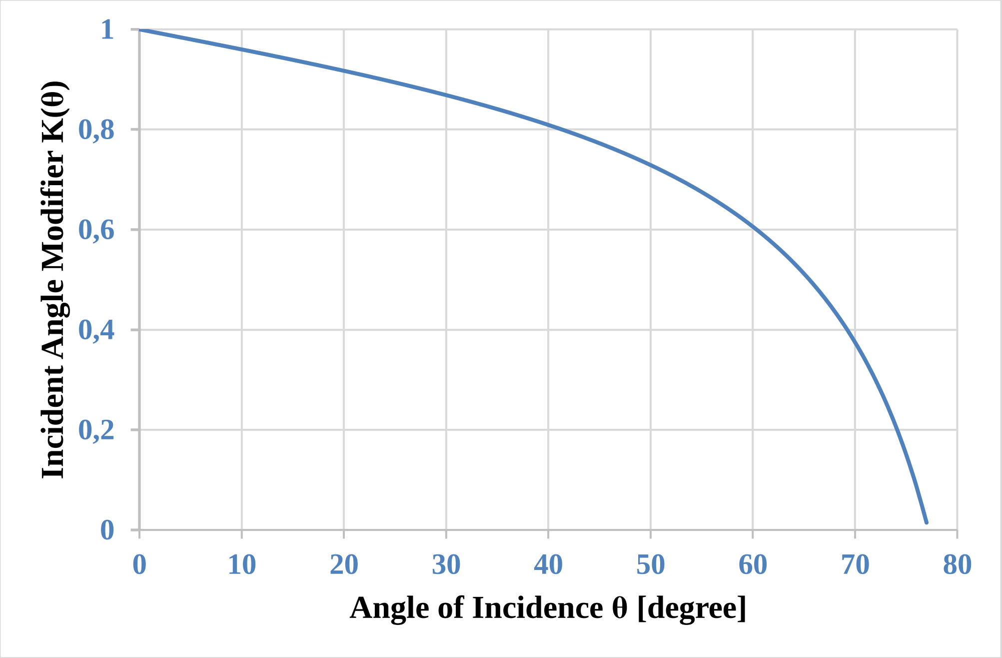

Figure 2.12. Incident angle modifier for different angles.

2.3.2. End Losses

With the change of incident angle, some solar beams do not hit to the receiver, and it causes a reducing in the optical efficiency. These areas at the edge of mirrors where reflected beams cannot reach to the receiver are described as end losses (effects). The distance of that ineffective part X shown in Figure 2.13 and the end losses term are defined as below [51]:

$$X = f \tan\theta \tag{2.25}$$

$$X_{end} = 1 - \frac{f}{L}\tan\theta \tag{2.26}$$

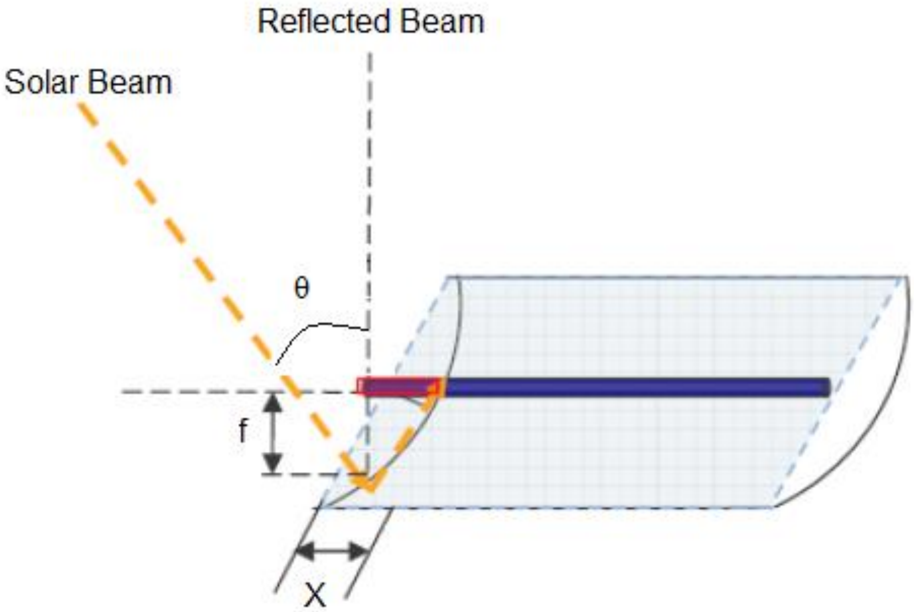

Figure 2.13. End losses.

2.3.3. Interception Factor

The interception factor is described as the reflected DNI by mirrors that intercepted by the receiver. Under perfect conditions that affect the interception factor, this value is equal to one. However, there are some errors related to these parameters either geometrical or manufactural in reality. The intercept factor is affected by the following parameters [46]:

- Receiver shadowing (γ_1)
- Tracking and twisting error (γ_2)
- Geometric accuracy of mirrors (γ_3)
- Dirt on mirrors (γ_4)
- Dirt on the receiver (γ_5)
- Unaccounted errors (γ_6)

By using these parameters, the interception factor can be calculated as following [46]:

$$\gamma = \prod_{j=1}^{6} \gamma_j \tag{2.27}$$

Moreover, it can be calculated using ray tracing method. Bartolato *et al*. [37] have calculated the intercept factor at different diameters of absorber tube shown in Figure 2.14.

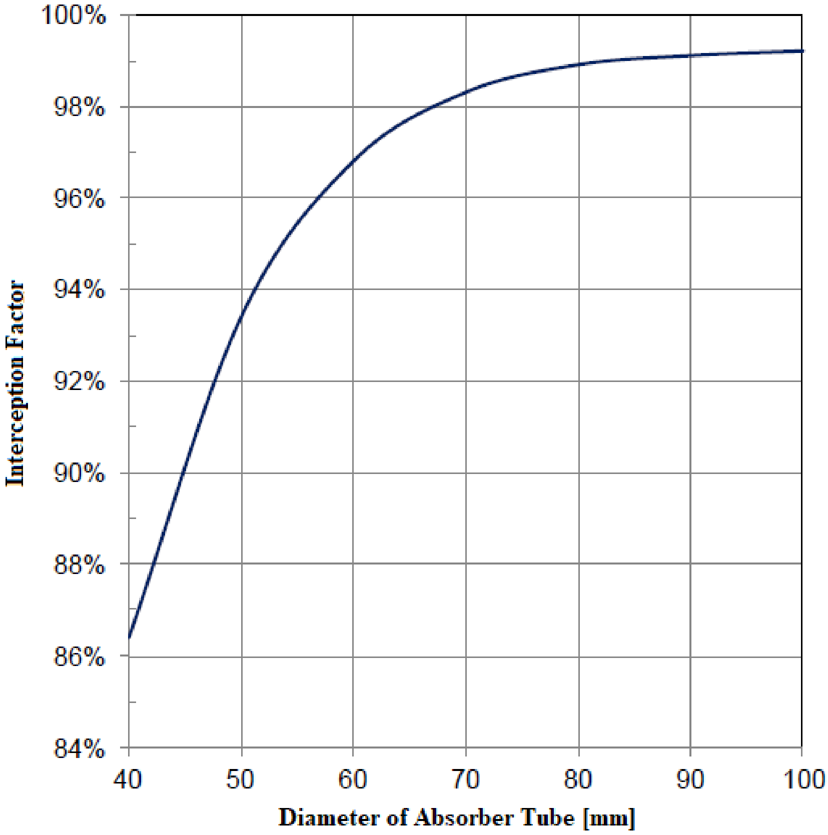

Figure 2.14. Change of interception factor with diameter of the absorber tube [37].

2.4. Thermal Analysis

The thermal analysis of the parabolic trough collector is necessary to define thermal efficiency, which is based on the energy balance of the collector and receiver. DNI incident on the collector, optical losses of the collector and receiver, thermal losses of the receiver, and the heat gain of HTF are included to evaluate the energy balance. 1-D energy balance provides reasonable outcomes for the receivers with short lengths, which are smaller than 100 m; however, 2-D energy balance is necessary for longer receivers [53]. In order to evaluate the thermal analysis, 1-D energy balance of the receiver should be described, and it is presented in Figure 2.15. The incoming solar radiation reflected from the collector, and it is absorbed by glass cover ($\dot{q}'_{5,\text{ sol-abs}}$) and absorber tube ($\dot{q}'_{3,\text{ sol-abs}}$). Most of this absorbed energy by absorber tube is conducted to the inner side of the tube ($\dot{q}'_{23,\ \mathrm{cond}}$) and then it is transferred by convection to HTF ($\dot{q}'_{12,\ \mathrm{conv}}$). Rest of the energy is conveyed back to glass cover by convection ($\dot{q}'_{34,\ \mathrm{conv}}$) and radiation ($\dot{q}'_{34,\ \mathrm{rad}}$). Also, there is a conduction heat loss ($\dot{q}'_{\mathrm{cond,\ bracket}}$) through the support bracket of the receiver. The energy transferred back is conducted by the class cover ($\dot{q}'_{45,\ \mathrm{cond}}$) and then it is convected ($\dot{q}'_{56,\ \mathrm{conv}}$) and radiated ($\dot{q}'_{57,\ \mathrm{rad}}$) to the environment as lost energy. Furthermore, a simplified illustration of the thermal resistance analysis is given in Figure 2.16 without incoming solar energy and optical losses.

The set of steady state energy balance equations for the four surfaces of the receiver starting from inside of absorber tube to outside of the glass cover respectively, considering heat fluxes are given below:

ri: $$\dot{q}'_{12,\ \mathrm{conv}} = \dot{q}'_{23,\ \mathrm{cond}} \tag{2.28}$$

ro: $$\dot{q}'_{3,\ \mathrm{sol\text{-}abs}} = \dot{q}'_{34,\ \mathrm{conv}} + \dot{q}'_{34,\ \mathrm{rad}} + \dot{q}'_{23,\ \mathrm{cond}} + \dot{q}'_{\mathrm{cond,\ bracket}} \tag{2.29}$$

gi: $$\dot{q}'_{34,\ \mathrm{conv}} + \dot{q}'_{34,\ \mathrm{rad}} = \dot{q}'_{45,\ \mathrm{cond}} \tag{2.30}$$

go: $$\dot{q}'_{45,\ \mathrm{cond}} + \dot{q}'_{5,\ \mathrm{sol\text{-}abs}} = \dot{q}'_{56,\ \mathrm{conv}} + \dot{q}'_{57,\ \mathrm{rad}} \tag{2.31}$$

$$\dot{q}'_{\mathrm{heat\text{-}loss}} = \dot{q}'_{56,\ \mathrm{conv}} + \dot{q}'_{57,\ \mathrm{rad}} + \dot{q}'_{\mathrm{cond,\ bracket}} \tag{2.32}$$

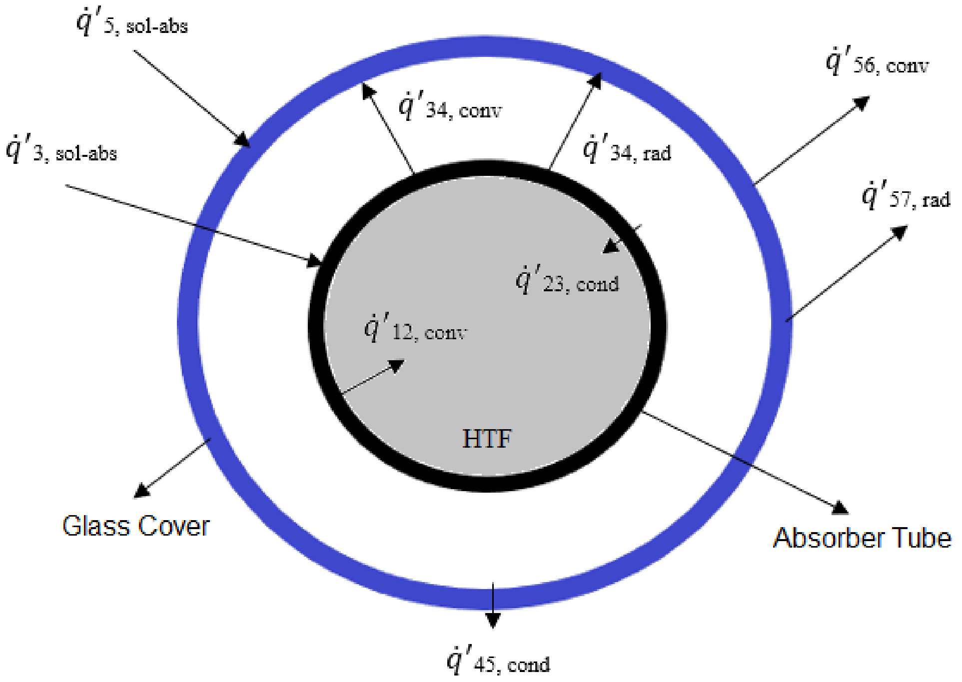

Figure 2.15. 1-D Energy balance of the receiver.

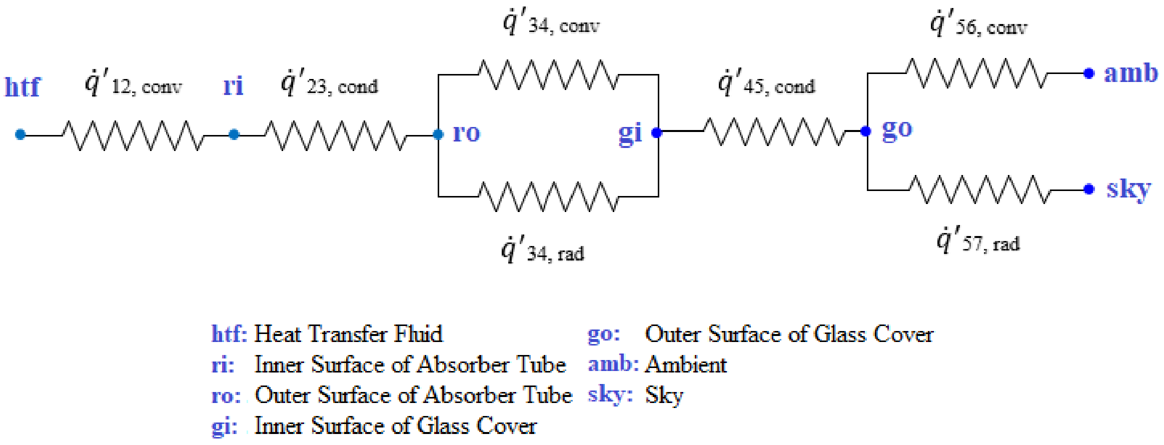

Figure 2.16. Thermal resistance analysis.

2.4.1. Convection Between the Absorber Tube and HTF

The convective heat transfer between the absorber tube and HTF can be expressed with the application of Newton’s Law of Cooling:

$$\dot{q}'_{12,conv} = h_{htf}\pi D_{ri}\left(T_{ri} - T_{htf}\right) \tag{2.33}$$

$$h_{htf} = \frac{Nu_{htf}k_{htf}}{D_{ri}} \tag{2.34}$$

where, T_{htf} is the average temperature of the HTF [K] and Nu_{htf} is Nusselt number at D_{ri}

In the one-dimensional energy balance analysis, all properties and temperatures are independent angularly and longitudinally of the receiver.

Definition of Nu number depends on the regime of flow in the absorber tube. The flow type is turbulent in some cases in the literature and my study. For the turbulent flow case (Re>2300), a correlation for Nu number is developed by Gnielinski [54]:

$$Nu_{htf} = \frac{(f_{ri}/8)(Re_{htf}-1000)Pr_{htf}}{1+12.7(f_{ri}/8)^{1/2}\left(Pr_{htf}^{2/3}-1\right)}\left(\frac{Pr_{htf}}{Pr_{ri}}\right)^{0.11} \tag{2.35}$$

$$f_{ri} = \left(1.82\log\left(Re_{htf}\right) - 1.64\right)^{-2} \tag{2.36}$$

$$Re_{htf} = \frac{\rho_{htf} V_{htf} D_{ri}}{\mu_{htf}} \tag{2.37}$$

This correlation for Nu_{htf} is valid for $2300 < Re_{htf} < 5x10^6$ and $0.5 < Pr_{htf} < 2000$ [37, 44]. Also, another formulation is developed to estimate friction coefficient with an implicit iterative formula of Colebrook [55]:

$$\frac{1}{\sqrt{f_{ri}}} = -2 \log\left(\frac{\xi / D_{ri}}{3.71} + \frac{2.51}{Re_{htf}\sqrt{f_{ri}}}\right) \tag{2.38}$$

If the Reynolds number is lower than 2300 (laminar flow), Nusselt number is independent from Prandtl and Reynolds, and equals to 4.36 [49]. Correlation graph for Nusselt and Reynolds Number with increasing temperature of HTF (25 to 100°C) at flow rates of 5 m^3/h shown in Figure 2.17. Also, correlation for the friction coefficient and HTF temperature (25 to 100°C) at the same flow rate shown in Figure 2.18.

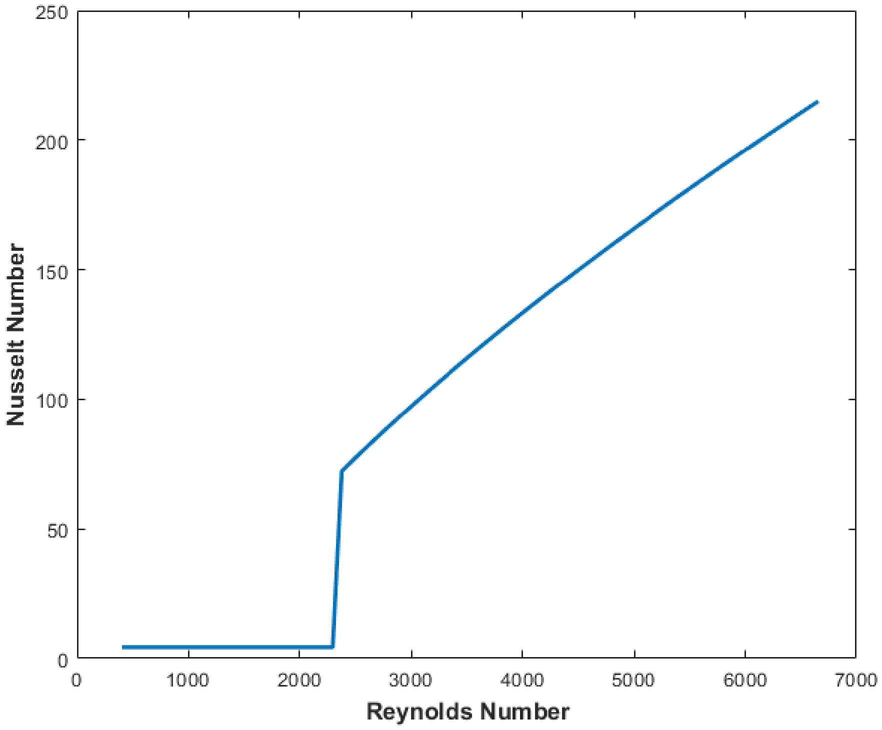

Figure 2.17. Nusselt-Reynolds number correlation.

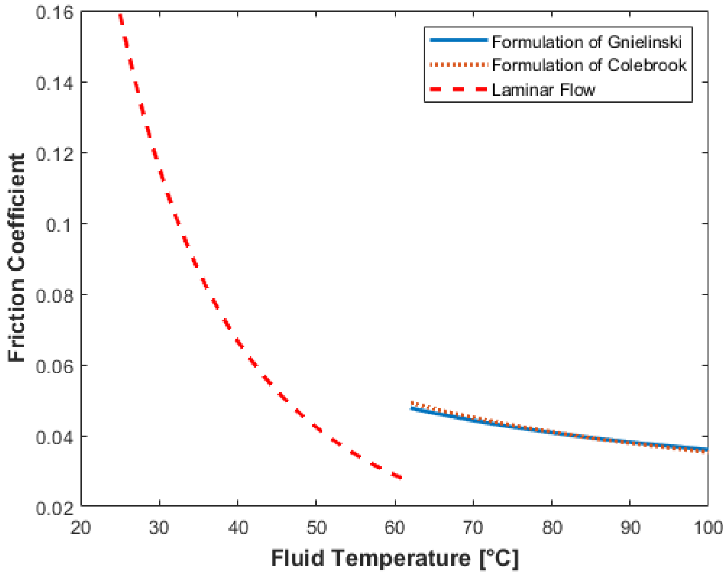

Figure 2.18. Correlation of friction coefficient and heat transfer fluid temperature.

2.4.2. Conduction Through the Absorber Tube Wall

Using the Fourier's Law, the conduction heat transfer through the wall of absorber tube can is calculated as following:

$$\dot{q}'_{23,cond} = \frac{2\pi k_r (T_{ri} - T_{ro})}{\ln(D_{ro}/D_{ri})} \tag{2.39}$$

where k_r is the thermal conductivity of the absorber tube at the mean temperature $(T_{ri}+T_{ro})/2$ [W/mK].

The thermal conductivity is a material property of the absorber tube. ASTM A160 GRB carbon steel is used as an absorber tube in the experimental setup. Thermal properties are given in Table 2.2, T is in the unit of °C.

Table 2.2. Material properties of the absorber tube.

Material of the absorber tube	Thermal conductivity [W/mK]	Density [kg/m³]	Specific heat [kj/kgK]
ASTM A160	-0.3664T+61.253	7861.09	0.0005T+0.4197

2.4.3. Convection Between the Absorber Tube and Glass Cover

The free molecular convection between the glass cover and absorber tube in vacuum condition can be expressed as [56]:

$$\dot{q}'_{34,conv} = h_{vac}\pi D_{ro}\left(T_{ro} - T_{gi}\right) \tag{2.40}$$

$$h_{vac} = \frac{k_{std}}{\left(D_{ro}/2\ln\left(D_{gi}/D_{ro}\right)\right) + b\lambda\left(D_{ro}/D_{gi} + 1\right)} \tag{2.41}$$

$$b = \frac{(2-a)(9\gamma - 5)}{2a(\gamma + 1)} \tag{2.42}$$

$$\lambda = \frac{2.331 \times 10^{-20}\left((T_{ro} + T_{gi})/2\right)}{p\delta^2} \tag{2.43}$$

$$Ra_{D_{gi}} = \frac{g\beta(T_{ro} - T_{gi}){D_{gi}}^3}{\nu\alpha} \tag{2.44}$$

where,

- h_{vac} is the convection coefficient for vacuum at the mean temperature $(T_{gi}+T_{ro})/2$ [W/m^{2}K]
- k_{std} is the thermal conductivity of vacuum at standard temperature and pressure [W/mK]
- γ is the ratio of specific heats in vacuum
- δ is the annulus gas molecular diameter [m]

These equations are valid with the condition of $\mathrm{Ra}_{\mathrm{D_{gi}}} < (\mathrm{D_{gi}}/(\mathrm{D_{gi}} - \mathrm{D_{ro}}))^{\,4}$. The constants can be found from the tables. Properties of air as an annulus gas is given in Tables 2.3 [49, 53].

Table 2.3. Heat transfer coefficient and constants for air [53].

Annulus Gas	k_{std} [W/mK]	b	λ [m]	γ [m]	δ [m]	h_{vac} [W/m^{2}K]
Air	0.02551	1.571	0.8867	0.0139	3.53x10^{-6}	0.0001115

In the condition of non-vacuumed receiver, the free convection between the glass cover and absorber tube is given as following [49]:

$$\dot{q}'_{34,conv} = \frac{2\pi k_{eff} L}{\ln\left(D_{gi}/D_{ro}\right)}\left(T_{ro} - T_{gi}\right) \tag{2.45}$$

$$\frac{k_{eff}}{k_{ann}} = 0.386\left(\frac{Pr_{ann}}{0.861 + Pr_{ann}}\right)\left(F_{cyl}Ra_{ann}\right) \tag{2.46}$$

$$F_{cyl} = \frac{\left[\ln\left(D_{gi}/D_{ro}\right)\right]^4}{\left[\left(D_{gi} - D_{ro}\right)/2\right]^3\left(D_{gi}^{-3/5} + D_{ro}^{-3/5}\right)^5} \tag{2.47}$$

where

- k_{ann} is the thermal conductivity of air for average temperature $(T_{gi}+T_{ro})/2$ [W/mK]
- Pr_{ann} is the Prandtl number of air for average temperature $(T_{gi}+T_{ro})/2$
- Ra_{ann} is the Rayleigh number of air for average temperature $(T_{gi}+T_{ro})/2$ and characteristic length of $(D_{gi}-D_{ro})/2$
- F_{cyl} is the form factor for concentric cylinders

These equations are valid with the condition of $0.70 \leq Pr_{ann} \leq 6000$ and $10^2 < F_{cyl} \cdot Ra_{ann} < 10^7$. If the product of F_{eyl} and Ra_{ann} is lower than 100, convection can be neglected and $k_{eff} = k_{ann}$.

2.4.4. Radiation Between the Absorber Tube and Glass Cover

The radiation heat transfer between the glass cover and absorber tube in can be expressed with some assumptions such as:

- Surfaces are gray
- Cylinders are concentric, isothermal and long
- There is no participation gas in the annulus (vacuum condition)
- Glass Cover is opaque
- Diffuse reflections and irradiations

Any error in calculations due to the assumptions above is relatively small. Therefore, following equation can be used for radiation:

$$\dot{q}'_{34,rad} = \frac{\sigma \pi D_{ro}\left(T_{ro}^4 - T_{gi}^4\right)}{\left(1/\varepsilon_r + (D_{ro}/D_{gi})\left(1-\varepsilon_g\right)/\varepsilon_g\right)} \tag{2.48}$$

2.4.5. Conduction Through the Glass Cover

The conduction heat transfer through the wall of glass cover is calculated by Fourier's Law same as conduction through the wall of absorber tube:

$$\dot{q}'_{45,cond} = \frac{2\pi k_g\left(T_{gi} - T_{go}\right)}{\ln\left(D_{gi}/D_{go}\right)} \tag{2.49}$$

where k_g is the thermal conductivity of the glass cover at the mean temperature $(T_{gi}+T_{go})/2$ [W/mK].

2.4.6. Convection from Glass Cover to Ambient

Natural convection in case of wind and forced convection without wind are two heat transfer mechanisms of convection from glass cover to ambient air. The former one causes the largest heat loss. The convective heat flux is expressed by Newton's law of cooling:

$$\dot{q}'_{56,conv} = h_{amb}\pi D_{go}\left(T_{go} - T_{amb}\right) \tag{2.50}$$

$$h_{amb} = \frac{Nu_{amb}k_{amb}}{D_{go}} \tag{2.51}$$

where k_{amb} is the convection coefficient of ambient air at $(T_{go}+T_{amb})/2$ [W/m^{2}K]. For the case of no-wind, Nu number correlations was defined by Churchill and Chu [53]:

$$Nu_{amb} = \left[0.6 + \frac{0.387 Ra_{D_{go}}^{1/6}}{(1 + (0.559/Pr_{amb})^{9/16})^{8/27}}\right]^2 \tag{2.52}$$

$$Ra_{D_{go}} = \frac{g\beta(T_{go} - T_{amb}){D_{go}}^3}{\nu\alpha} \tag{2.53}$$

$$\beta = \frac{1}{\left(T_{go} + T_{amb}\right)/2} \tag{2.54}$$

$$Pr_{amb} = \frac{\nu}{\alpha} \tag{2.55}$$

These equations are valid with the condition of $10^5 < \mathrm{Ra}_{\mathrm{D_{go}}} < 10^{12}$.

For the windy case, the Nusselt number can be expressed with the following equation [49]:

$$Nu_{amb} = 0.3 + \frac{0.62 Re_{amb}^{1/2} Pr_{amb}^{1/3}}{(1 + (0.4/Pr_{amb})^{2/3})^{1/4}} \left[1 + \left(\frac{Re_{amb}}{282000}\right)^{5/8}\right]^{4/5} \tag{2.56}$$

where $\mathrm{Re_{amb}}$ is the Reynolds number for $(\mathrm{T_{go}}+\mathrm{T_{amb}})/2$ at $\mathrm{D_{go}}$. The correlation above is valid for $\mathrm{Re_{amb}} \cdot \mathrm{Pr_{amb}} > 0.2$.

2.4.7. Radiation from Glass Cover to the Sky

The radiative heat transfer from glass cover to the sky is caused by the temperature difference between the outer temperature of absorber tube and the sky. In this scenario, absorber tube is a small gray object and sky is a large blackbody. Therefore, the net radiative heat flux from glass cover to the sky can be defined as:

$$\dot{q}'_{57,\mathrm{rad}} = \sigma\pi D_{go}\varepsilon_g\left(T_{go}^4 - T_{sky}^4\right) \tag{2.57}$$

A relation can be written for $\mathrm{T_{sky}}$ with the temperature of dry bulb $\mathrm{T_{air}}$ and the ambient dew point temperature $\mathrm{T_{dp}}$ as following [41, 50]:

$$T_{sky} = \varepsilon_{sky}^{1/4} T_{air} \tag{2.58}$$

and the sky emissivity is:

$$\varepsilon_{sky} = 0.711 + 0.56\frac{T_{dp}}{100} + 0.73\left(\frac{T_{dp}}{100}\right)^2 \tag{2.59}$$

Figure 2.19 shows the change of the sky emissivity with the dew point temperature. The sky emissivity was around 0.85 during the experiments.

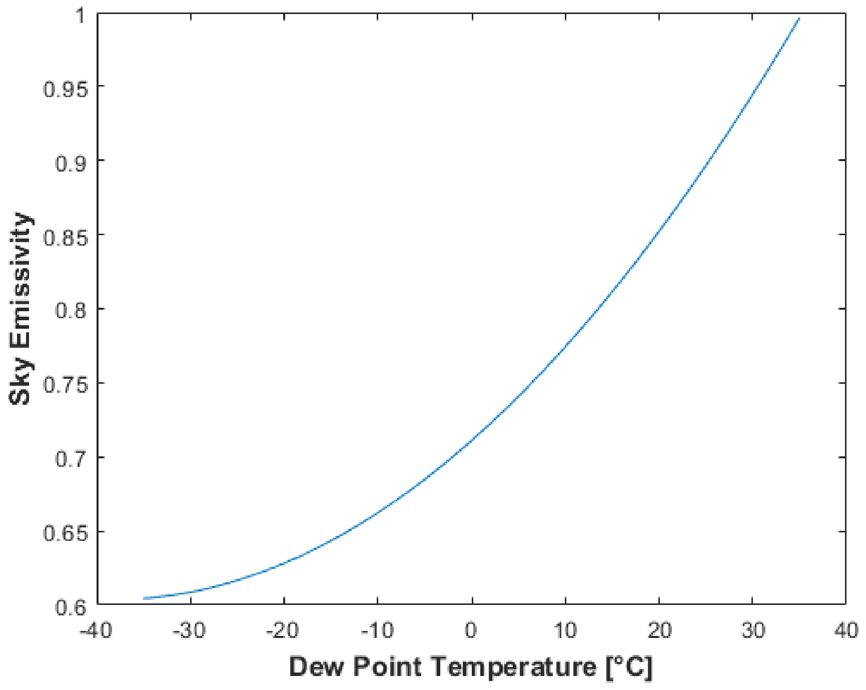

Figure 2.19. Change of sky emissivity with dew point temperature.

2.4.8. Thermal Efficiency

The useful heat gain can be calculated using the temperature difference between inlet (T_{in}) and outlet (T_{out}) of the absorber tube as following:

$$\dot{Q}_{useful} = \dot{m}_{htf} c_{htf} (T_{out} - T_{in}) \tag{2.60}$$

where $\dot{m}_{htf}$ is the mass flow rate of HTF [kg/s].The available solar energy coming to the solar collector (Q_{solar}) is another definition to express thermal efficiency:

$$\dot{Q}_{solar} = G_b A_c \tag{2.61}$$

Therefore, the thermal efficiency of PTC (η_{th}) can be calculated with the ratio of definitions above as:

$$\eta_{th} = \frac{\dot{m}_{htf} c_{htf} (T_{out} - T_{in})}{G_b A_c} \tag{2.62}$$

The energy balance of cylindrical absorber tube can be expressed under steady state condition as below:

$$\dot{Q}_{solar} = \dot{Q}_{useful} + \dot{Q}_{loss} \tag{2.63}$$

$$\dot{Q}_{loss} = U_L A_r (T_r - T_{amb}) \tag{2.64}$$

where S is the collected solar beam radiation [W], T_r is the mean temperature of absorber tube. The overall heat loss is defined to relate all thermal losses with one coefficient. A correlation for the overall heat loss coefficient is expressed by Kalogirou [19]:

$$U_L = \left[\frac{A_g}{A_r\left(h_{amb} + h_{g-amb,rad}\right)} + \frac{1}{h_{vac} + h_{r-g,rad}}\right]^{-1} \tag{2.65}$$

where $h_{r-g,rad}$ is the radiation coefficient from absorber tube to glass cover, and $h_{g-amb,rad}$ is the radiation coefficient from glass cover to ambient. These coefficients are described as [19, 24]:

$$h_{r-g,rad} = \frac{\sigma\left(T_r + T_g\right)\left(T_r^2 + T_g^2\right)}{\left(\frac{1}{\varepsilon_r} + \frac{A_r}{A_g}\left(\frac{1}{\varepsilon_g} - 1\right)\right)} \tag{2.66}$$

$$h_{g-amb,rad} = \sigma \varepsilon_g \left(T_g + T_{sky}\right)\left(T_g^2 + T_{sky}^2\right) \tag{2.67}$$

where T_g is the mean temperature of glass cover.

The heat removal factor (F_R) of PTC is another definition and used to calculate the total useful heat gain. The formulation for the heat removal factor is given as the ratio of the actual useful heat gain to the gained energy when the whole absorber tube is at the inlet temperature of the HTF (T_{in}) [49]:

$$F_R = \frac{\dot{m}_{htf} c_{htf}}{A_r U_L}\left[1 - exp\left(-\frac{A_r U_L F'}{\dot{m}_{htf} c_{htf}}\right)\right] \quad (2.68)$$

$$F' = \frac{1/U_L}{\frac{1}{U_L} + \frac{D_{ro}}{h_{htf} D_{ri}} + \frac{D_{ro}\ln(D_{ro}/D_{ri})}{2k_r}} \quad (2.69)$$

where F' is the efficiency factor of PTC. By using these definitions above, thermal efficiency is expressed as following [49]:

$$\eta_{th} = F_R\left[\eta_{op} - \frac{U_L}{C}\left(\frac{T_{in} - T_{amb}}{G_b}\right)\right] \quad (2.70)$$

3. PARABOLIC TROUGH COLLECTOR SYSTEM

3.1. The Setup

Parabolic trough collector test system is designed and installed with the aim of performance assessment at BURET (Boğaziçi University Renewable Energy Technologies) Laboratory, Boğaziçi University's Sarıtepe Campus, Turkey. The test setup consists of a support system, mirrors, a solar tracking system, an absorber tube and glass cover, piping for circulation of HTF, a boiler, a pump, an expansion tank, valves, and measurement equipment such as thermocouple and flowmeter. The piping and instrumentation diagram is given in Figure 3.1.

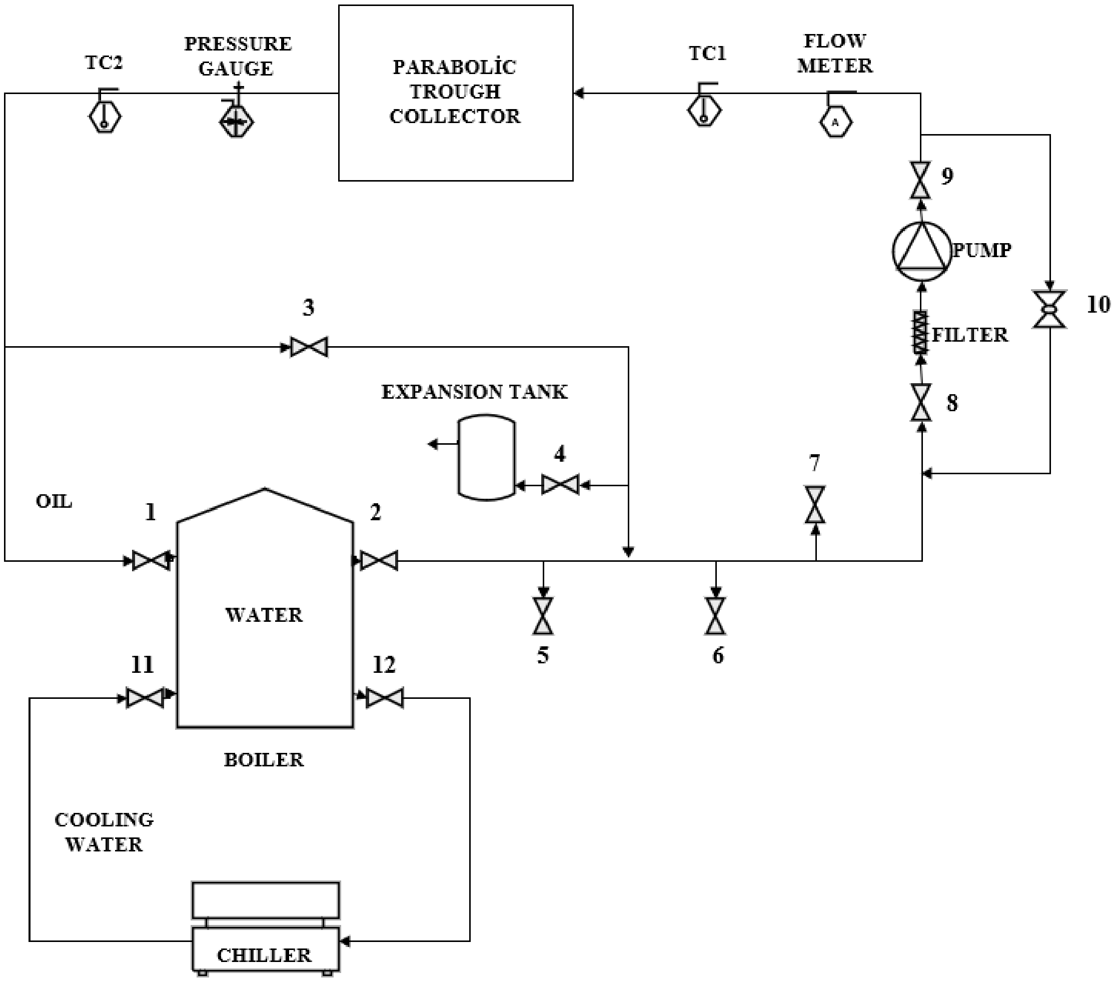

Figure 3.1. Piping and instrumentation diagram of the system.

Also, the 3D model view and the photograph of the experimental test setup is shown in Figure 3.2 and Figure 3.3, respectively.

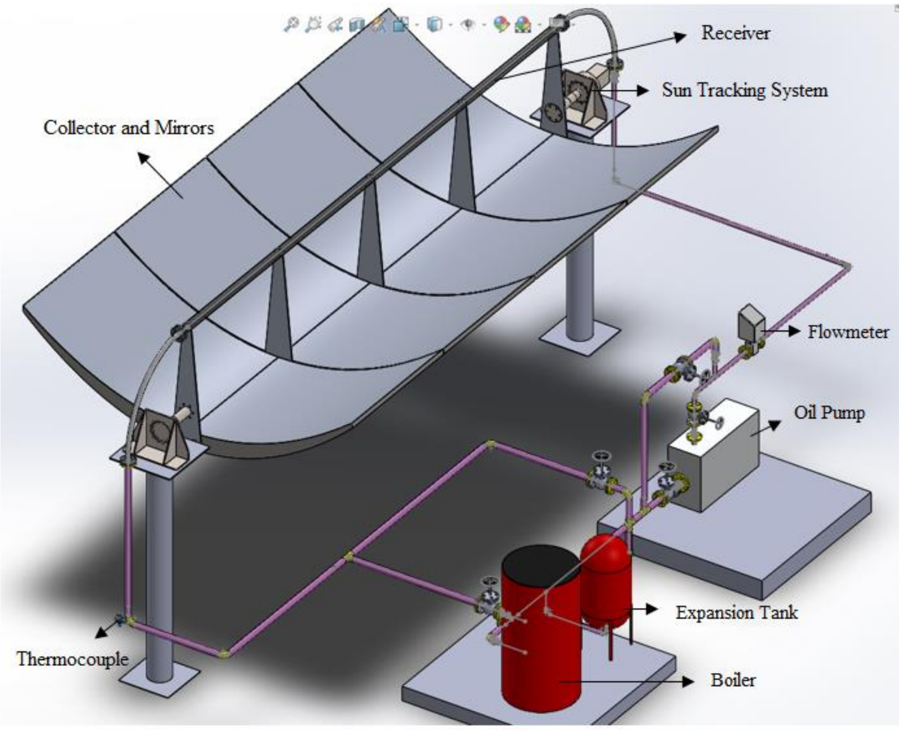

Figure 3.2. 3D Model view of the experimental test setup.

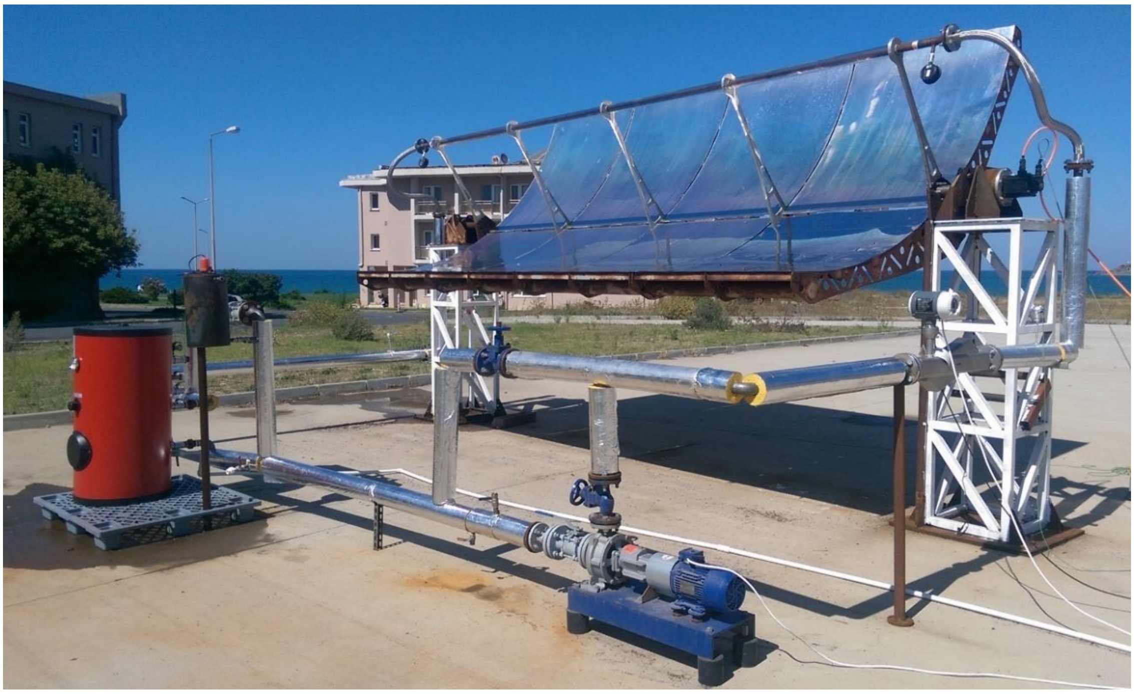

Figure 3.3. Experimental test setup of PTC.

3.1.1. Reflectors/Mirrors

The reflectors/mirrors on the parabolic trough concentrate the solar radiation upon the receiver with high reflectivity. A polished aluminum sheet was used as a reflector with dimensions of 125x160 cm and thickness of 1 mm. The reflectivity of material is 0.9. The advantages of this kind of reflector are high reflectivity, light weight, and low cost. However, there is no protection from weather conditions, and an accurate parabolic structure is required [58].

3.1.2. The Receiver

The receiver consists of a pipe called absorber tube and a glass cover around. The HTF circulates in this absorber tube. Therefore, the absorber tube has to be durable against the high temperature of HTF. ASTM A160 GR.B was used for piping of the oil cycle of the system. It is a seamless carbon steel pipe. It is generally painted black to increase the absorption of solar radiation and minimize emissions of radiation. The outside diameter of the absorber tube is 48.3 mm with 3.7 mm thickness. The absorptivity of the tube is 0.88. The thermal conductivity of the absorber tube was given in the previous chapter.

With the aim of reducing heat losses because of the heat transfer mechanisms of conduction, convection, and radiation, a glass cover was used around the absorber tube. The used glass cover is the SCHOTT company’s DURAN® product. The transmissivity of the product is 0.9, and the absorptivity is 0.02 [59].

Figure 3.4. The receiver.

3.1.3. Oil Circulation System

Renolin Therm 320 was used as the heat transfer fluid (HTF) due to its advantages of working temperature, high availability, and low cost. The properties of Renolin Therm 320 is given in Table 3.1. Moreover, some advantages are listed below:

- Protects against corrosion,
- It has decent heat transfer properties,
- It has an extended service life,
- The permissible film temperature is 320°C.

Table 3.1. Properties of Renolin Therm 320 [60].

Temperature [°C]	Density [kg/m³]	Specific heat [kj/kgK]	Heat conductivity [W/mK]	Kinematic viscosity [m²/s] E-06
0	879	1,864	0,134	535
50	848	2,078	0,131	28,6
100	816	2,293	0,127	6,5
200	750	2,721	0,120	1,5
300	685	3,151	0,113	0,7
320	672	3,236	0,111	0,6

The HTF circulation pump is selected according to the flow rate and pressure of the system. KSB company’s Etanorm pump shown in Figure 3.5 is used for oil circulation in the system. The suction port of the pump is DN50 and the outlet port is DN32. The maximum volumetric flow rate provided by the pump is 12,5 m³/h at 2900 rpm. The dimensions are 30x50x40 cm. The pump is controlled with Delta’s VFD-E frequency inverter to adjust rpm so the flow rate in need.

Figure 3.5. Oil circulation pump.

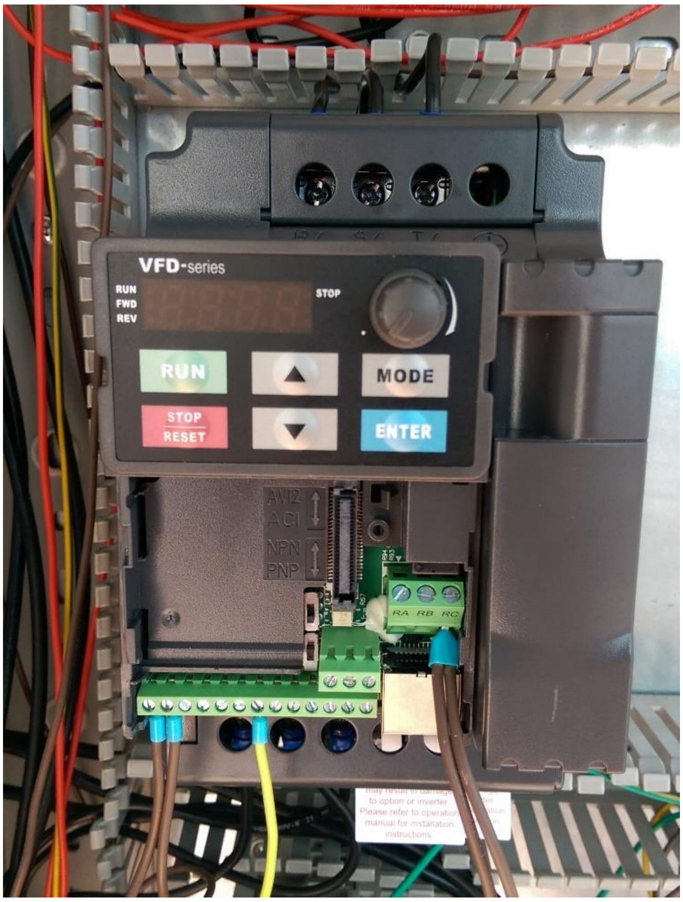

Figure 3.6. Variable frequency driver of the pump.

With an increase in temperature, the density of fluid decreases; correspondingly, the volume of the fluid increases in the system. In order to compensate this increase in the system, an open expansion tank was used with a capacity of 20 liters.

Figure 3.7. Expansion tank.

3.1.4. Water Circulation System

Tanpera’s TDB 160/10 dual coil boiler tank illustrated in Figure 3.8 is used as the heat storage and a heat exchanger in the system. The capacity of the tank is 160 liters, the diameter is 600 mm, and the height is 1130 mm. A safety valve is used at the inlet of cold water. One of the coils was used for the circulating of cold water, and the heat transfer oil circulated in the other one. For the cooling cycle, an air-cooled chiller which had two hermetic scroll-type compressors inside was integrated to the system to supply cold water. Specifications of the chiller are given in Table 3.2. This cooling system is put into use when the water temperature exceeds 90°C because boiling water inside the boiler creates malfunctioning.

Table 3.2. Specifications of the chiller.

Maximum cooling capacity [kW]	107
Evaporator type	Shell and tube
Flow rate of water in evaporator [m^3/h]	18.5
Power supply	400 V/3 phase/50 Hz
Number of fans	2
Flow rate of air at fans [m^3/h]	34500
Nominal power of pump [kW]	4
Water tank volume [lt]	350

Figure 3.8. Boiler.

Figure 3.9. Chiller.

3.1.5. Measurement Devices

The measurement devices in the system are thermocouples for temperature measurement, a flowmeter for flow measurement, and a velocity transmitter for wind speed and temperature measurement. For the temperature measurement, Elimko’s MI01-1K60-16-G NiCr-Ni K-type thermocouple shown in Figure 3.10 is used. The thermocouples are mounted by mounting bushes to the piping to measure inlet and outlet temperatures of the PTC. One of them is mounted to the boiler to control water temperature. The material of protecting tube is 316Ti stainless steel and the range of temperature measurement is between -60°C and 1370°C [61]. However, these thermocouples do not show the temperature data on them due to the lack of a digital screen. Therefore, a dial thermometer of Pakkens company (TE 100) is added to the outlet of the collector for direct reading of the outlet temperature. Its scale range is 0°C to 160°C and the material of protecting tube is AISI 316 stainless steel [62]. Moreover, a pressure gauge of the Pakkens is mounted to the outlet of the collector; its scale range is 0 to 10 bars.

Figure 3.10. K-type thermocouple.

Figure 3.11. Coriolis flowmeter.

For the flow measurement, ABB's FCM2000 CoriolisMaster illustrated in Figure 3.11 is used. In order to withstand high oil temperatures, the material of sensor and sensor housing is made of AISI 316Ti stainless steel. The permissible measuring medium temperature range is -50°C to 200°C. This flowmeter has the following advantages [63]:

- accuracy of the flow rate is ±0.15% of maximum flow rate,
- accuracy of density is ±5 g/l,

- reproducibility of flowrate is 0.1%,
- reproducibility of density is ±0.1 g/l,
- the operation is through the front glass via capacitive buttons, there is direct reading,
- there are common electronic components and Piezo sensors for all nominal diameters and applications
- the measurement accuracy of the temperature is ±1°C or 1% of the measured value (in °C), whichever is greater.

Furthermore, the solar radiation data for the whole year is recorded at the university's wind turbine meteorology center, hence the data can be obtained there. The ambient temperature and the wind speed are measured experimentally with the E+E ELEKTRONIK EE75 air velocity transmitter illustrated in Figure 3.12. It has high accuracy up to 40 m/s in the temperature range of -40 to 120°C [64].

Figure 3.12. Velocity Transmitter.

3.1.6. Sun Tracking System

In order to maximize the incident energy from the sun, the PTC is placed to the east-west direction and rotates around the north-south axis through a PLC solar tracking system. The solar tracking system consists of a servomotor, a driver, and a PLC controller. An AC servo motor of Delta Electronics with a capacity of 1.5 kW, 2000 rpm with an electromechanical brake is implemented to the system to drive the PTC. Also, the same company's AC driver ASDA-B and the PLC controller DVP-14SS2 are used to program the movement of servomotor shown in Figure 3.13. The PLC program runs with fixed-rate angular correction, and it provides 15 degrees rotation about the aforementioned axis in an hour, and this equals to the movement of the Sun. Experiments were performed between 10 AM and 3 PM. Therefore, the collector was set to 60 degrees at the start with the east-west axis. Codes are written to PLC with WPLSoft and rotations are controlled via control panel buttons.

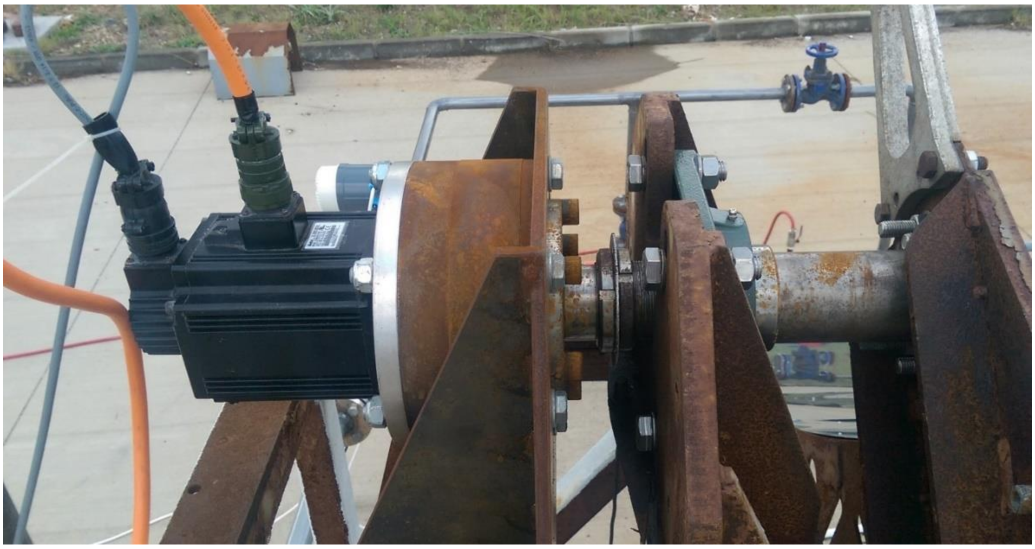

Figure 3.13. Sun tracking mechanism.

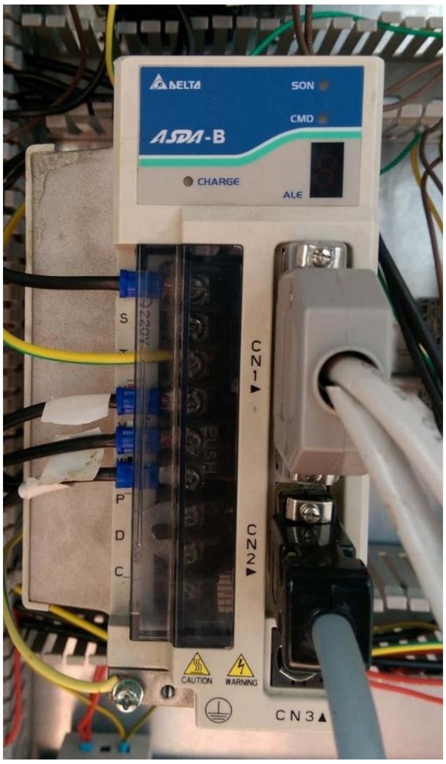

Figure 3.14. AC driver of servomotor.

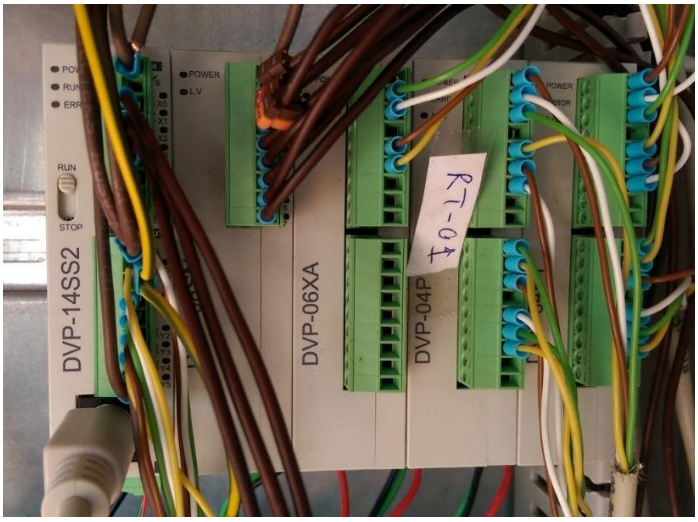

Figure 3.15. PLC controller.

3.1.7. Data Acquisition System

A data acquisition system of IPETRONIK is adapted to the measurement system. The system has two modules that are M-THERMO2 and M-SENS 8 shown in Figure 3.16. The former one collects the temperature data from type K thermocouples. The latter one collects voltage, current, and sensor signals with sensor excitation; these two modules are connected to the computer to recover the data.

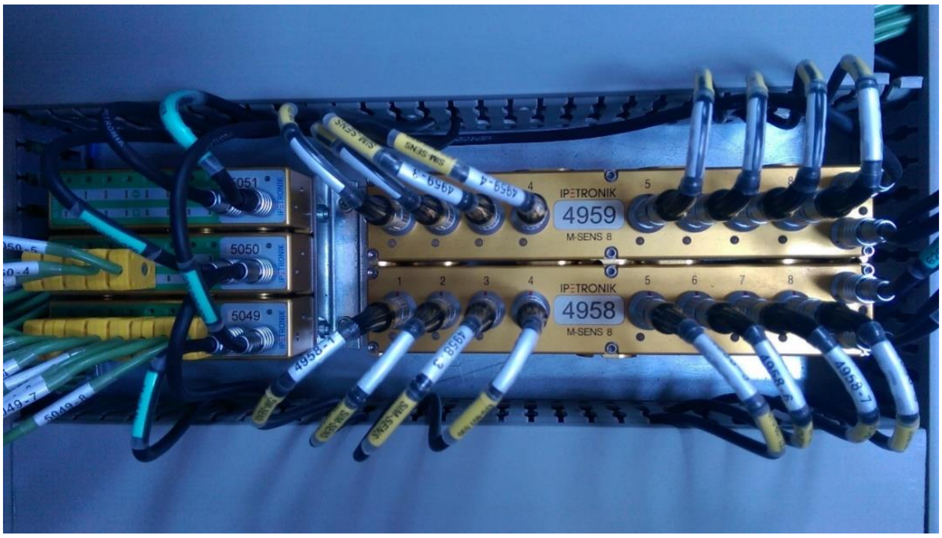

Figure 3.16. M-THERMO2 and M-SENS 8 modules of the data acquisition system.

3.2. Experimental Procedure

Experiments were conducted at Sarıtepe Campus, where the average daily direct normal irradiation is 533 W/m² in July. The average ambient temperature is 23.7°C.

There are two main cycles applied for experiments. In the first cycle shown in Figure 3.17, the boiler is bypassed using the corresponding valves and oil is heated without cooling, inlet and outlet temperatures of the collector are recorded to analyze the maximum heating capacity of the PTC. If the oil temperature reaches close to the ignition temperature, the pump should be stopped and the collector should be rotated to the shade. This is called Experiment I.

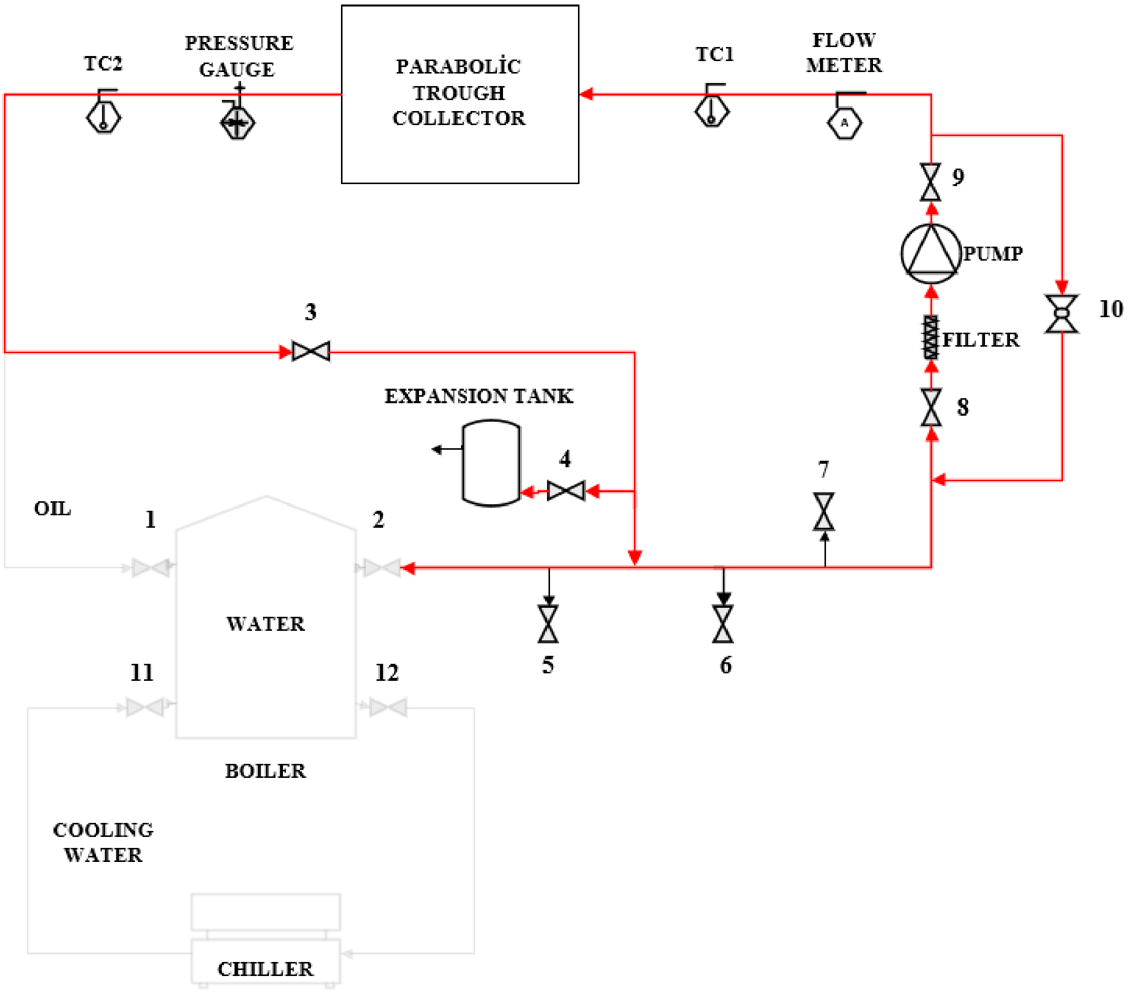

Figure 3.17. Flow cycle for the Experiment I.

In the second cycle shown in Figure 3.18, there is no bypass; the boiler is filled to full capacity, with water at ambient temperature. The heated oil circulates in the heat exchanger of the boiler to transfer its heat to water, so the water temperature goes up. Should the desired water temperature of 90°C (also the limit temperature for boiler) be reached, cooling is required to prevent a further rise in water temperature. This is called Experiment II.

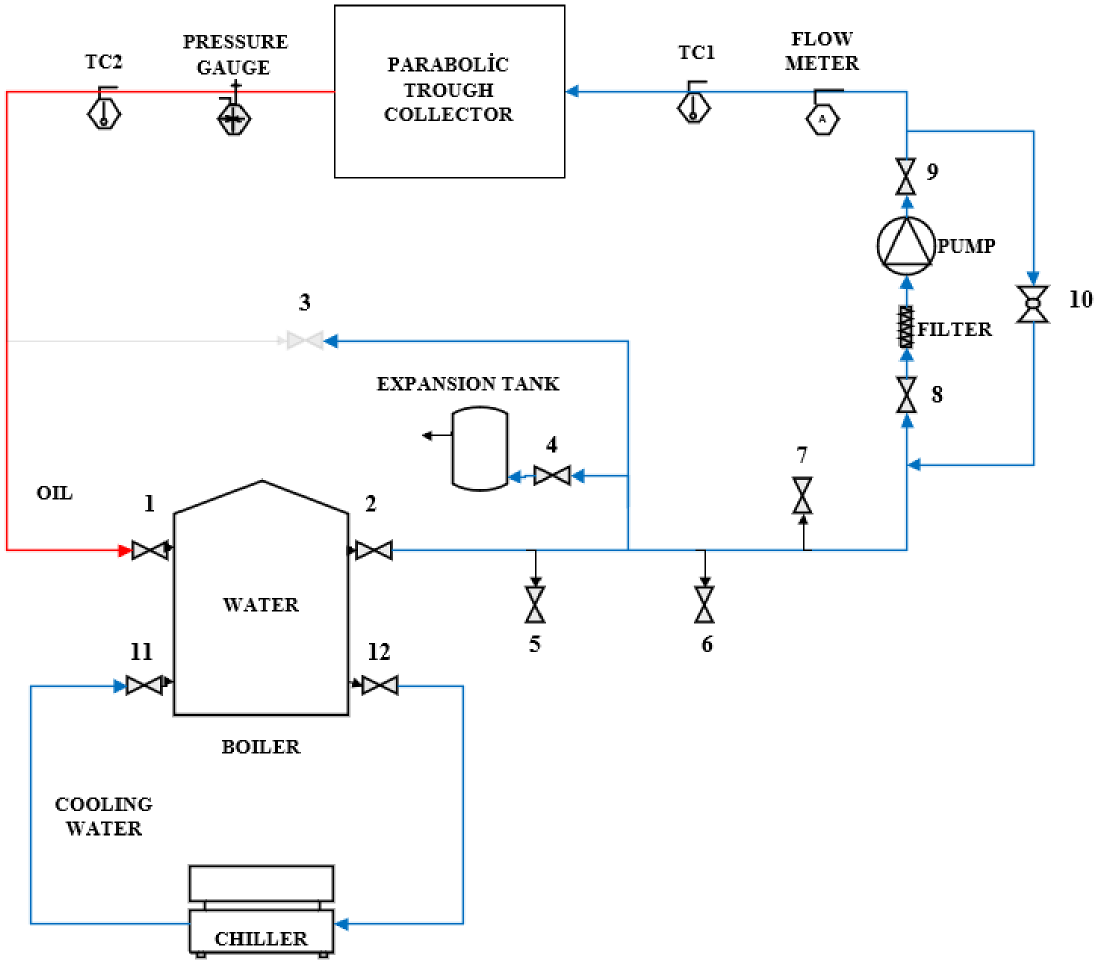

Figure 3.18. Flow cycle for the Experiment II.

Volumetric flow rates are adjusted either with the inverter or the bypass line of the pump. In the Experiment I, a constant volumetric flow rate is set to 5 m³/h, with 40 Hz frequency of pump motor. In Experiment II, flow rates of 3.5 m³/h, 4.15 m³/h, 5 m³/h, 6.75 m³/h are obtained with 25 Hz, 30 Hz, 40 Hz, and 50 Hz, respectively. Thus, laminar and turbulent flows can be observed in the system. The whole system is controlled from the control panel, and there is also an emergency stop button.

Before the experiments, the system is filled with heat transfer fluid using valve 7. Also, the air in the system should be drained using an air relief valve.

The test procedure of Experiment I is given below:

(i) Close the following valves: 1,2,5,6,7,10,11,12,
(ii) Open the following valves: 3,4,8,9,
(iii) Turn on the data system and start recording,
(iv) Adjust the position of the collector for minimum incident angle and then run the servomotor for sun tracking mechanism,
(v) Run the HTF pump with 40 Hz,
(vi) Observe the temperature difference between inlet and outlet, and the flowrate,
(vii) Read the values from software on the computer, T_{max} =200°C,
(viii) If the system reaches the max temperature, start cooling,
(ix) Stop the HTF pump.

The test procedure of Experiment II is as follows:

(i) Repeat Experiment I until the fluid reaches 100°C,
(ii) Open valves 1 and 2, and close valve 3,
(iii) Read the water temperature in the thermal storage tank, T_{max} =90°C,
(iv) If the water temperature reaches the maximum value in boiler, start the chiller for cooling water,
(v) Keep the constant temperature at the thermal storage tank.

Both experiments can be performed at different flow rates to evaluate the effects of different flow conditions. The flow rates can be adjusted using frequency invertor of pump or bypass valve if necessary.

4. RESULTS AND DISCUSSIONS

In this part of the thesis, the test results of PTC test setup are presented. Experiments are conducted at BURET, on Sarıtepe Campus of Boğaziçi University in July, between 10:00 A.M. and 5:15 P.M. The data acquisition system has stored the data of measurements with the 1 Hz frequency.

4.1. Solar Radiation

The solar radiation data do not meet desired conditions for continuous healthy measurements on test days because the sky was partly cloudy and the weather pattern was very unstable in July; the sunlight was interrupted by clouds at some points during the tests.

The location of the test setup generally receives abundant solar radiation in summertime. The yearly average of direct normal radiation is 1260 kWh/m² at the location (N 41° 14' 38", E 29° 00' 47"). The radiation data were expected from the measurement devices located on the wind turbine. However, the measurement devices were under maintenance during experiment days. Therefore, the average solar radiation data are used instead for calculations. The average solar radiation data in July are given in Figure 4.1. The average peak solar intensity in July is 958 W/m² at 12:10.

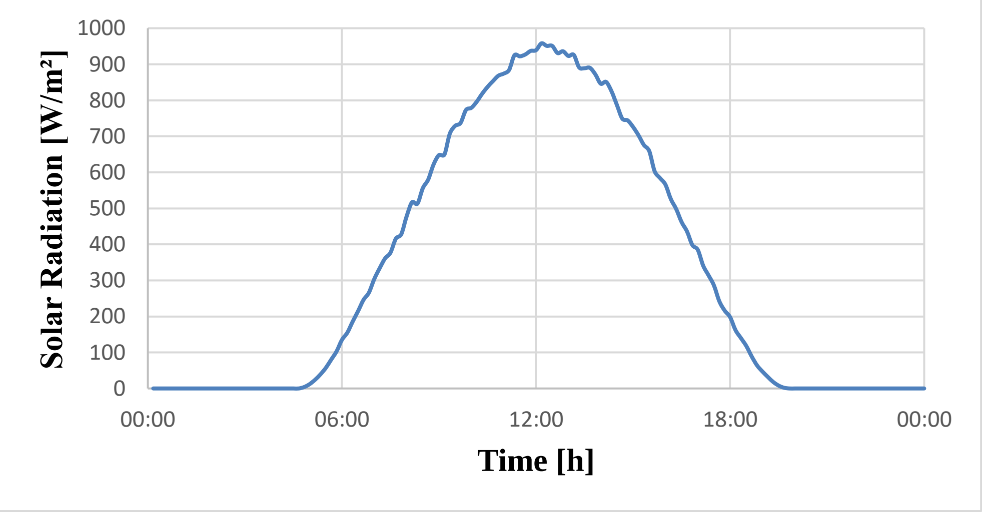

Figure 4.1. Average solar radiation data of July [65].

4.2. Ambient Conditions

The ambient conditions are significant on the thermal performance of the PTC because they affect the heat loss especially through convection and radiation.

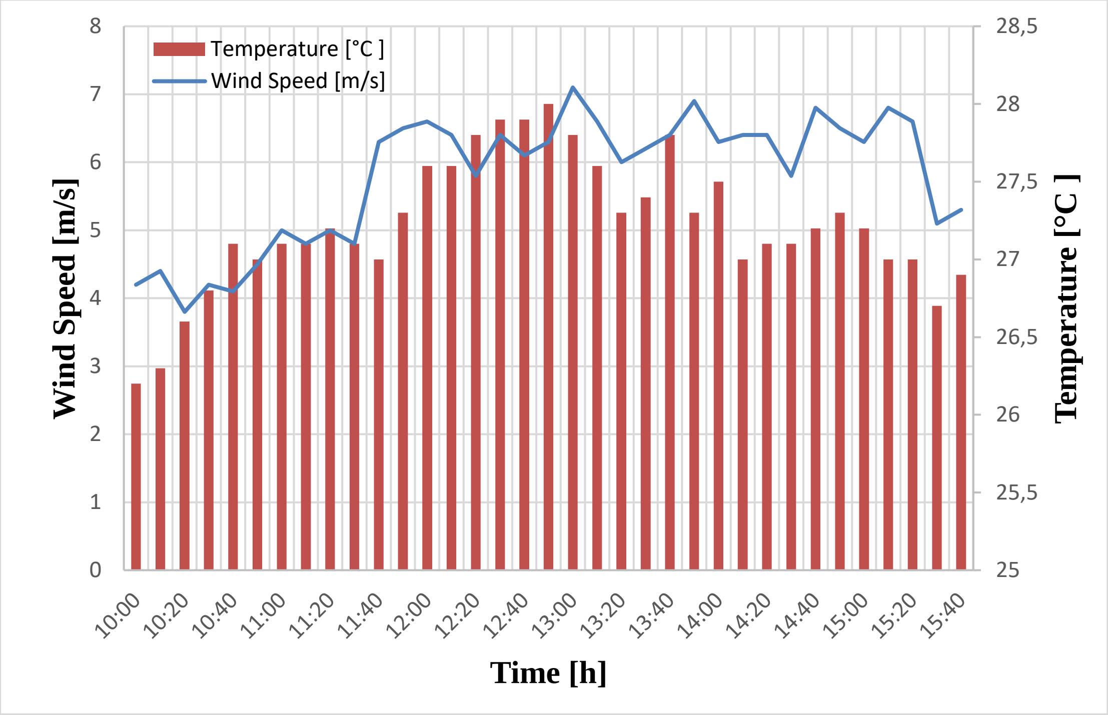

Figure 4.2. Ambient temperature and wind speed.

The daily variation of ambient temperature and wind speed is illustrated in Figure 4.2. The data were collected using an anemometer. As shown in the figure, the average ambient temperature was 27.2°C with a maximum temperature of approximately 28°C, and the average wind speed was 5.8 m/s with a peak value of 7.1 m/s on the day of measurements used for this report. The wind speed is pretty high in the region and it results in high heat losses of the system.

4.3. Inlet and Outlet Temperatures

Measurements of the inlet and outlet temperatures are one of the main objectives to evaluate the thermal performance of the PTC. The change in temperatures with respect to time for the Experiment I is given in Figure 4.3.

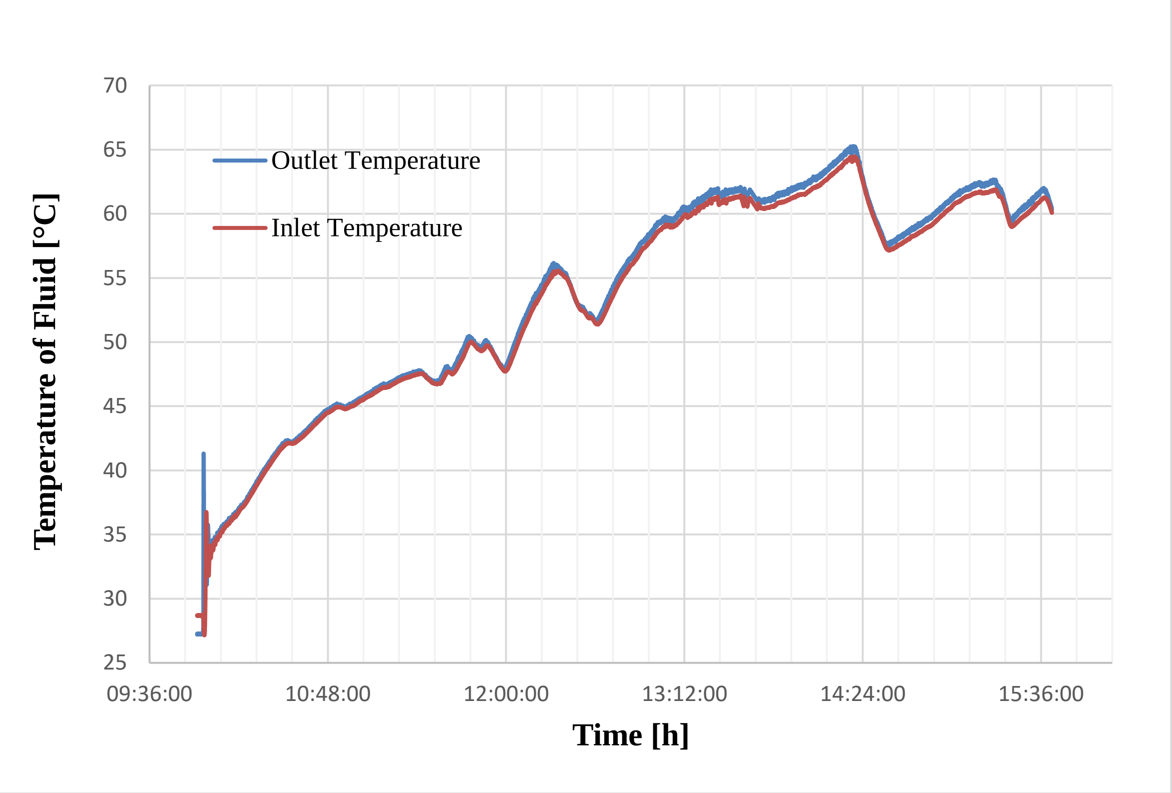

Figure 4.3. Inlet and outlet temperatures.

A peak temperature of 65.25°C was obtained at 14:20. The temperatures were fluctuating during the experiment due to moving clouds. Without sunlight above PTC due to the clouds and high wind speeds, the temperatures decreased at some points around 12:20 and 14:20. Although temperatures increased, the difference between the inlet and outlet temperature, which is significant for the thermal efficiency calculation, was narrow. An expected of over 100°C could not be observed in the system; there were some reasons for this problem: the first reason for this was the weather conditions; because it was windy and cloudy. Another reason was the mass flow rate. The mass flow rate was chosen to be between 65 to 70 kg/min, which resulted in small. The flow rate was mostly steady during measurements; the change in the mass flow rate can be seen in Figure 4.4. Also, the low absorptivity of the absorber tube, the misalignment of the receiver, the dirt on mirrors, and tracking errors were the reasons for low optical efficiency and interception factor, so the temperature difference.

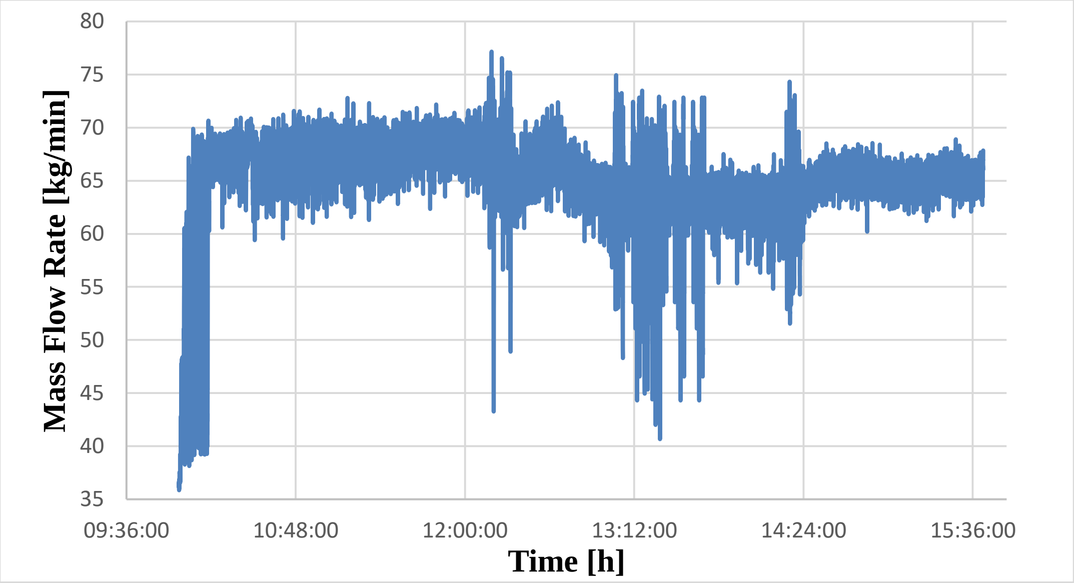

Figure 4.4. Mass flow rate of HTF.

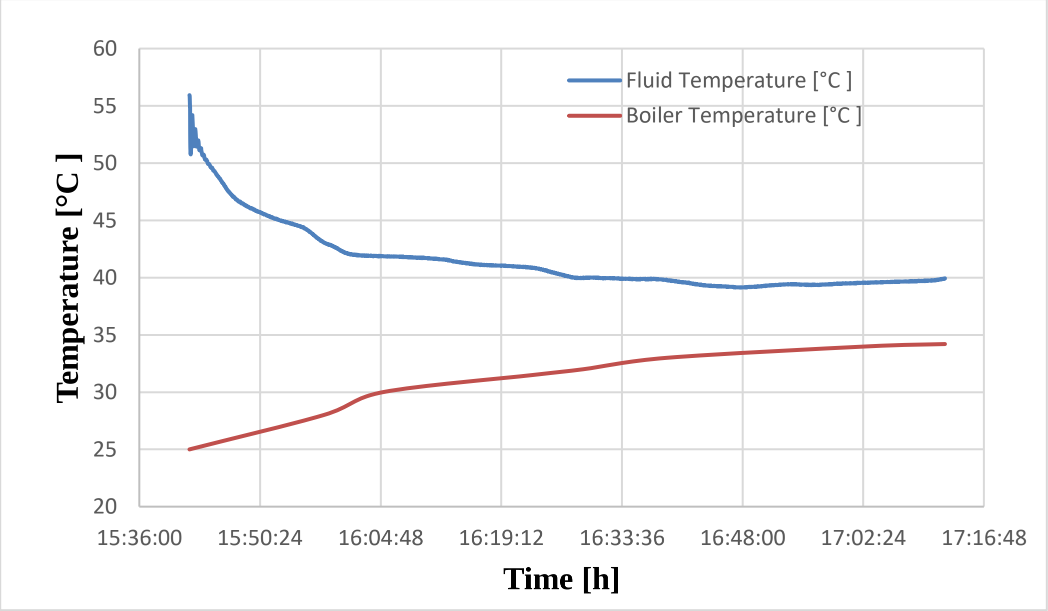

Figure 4.5. Temperatures for Experiment II.

After 3:40 P.M., Experiment II was carried out following the necessary procedure outlined. The HTF was circulated throughout the coil of the boiler to exchange heat with the water inside the boiler. The gap between HTF temperature and the boiler temperature was decreased as shown in Figure 4.6 from 30°C to 5°C. The sky was mostly cloudy at that hour so that justified the results. The cooling from the chiller was not required at that point.

4.4. Useful Heat Gain

The useful heat gain was calculated with using the temperature difference of inlet and outlet, mass flow rate and specific heat as presented in equation 2.62. The average change in Q_{useful} is plotted in Figure 4.6. The peak value is obtained to be 1694 W at around 14:10, where the HTF temperature was at the peak as well.

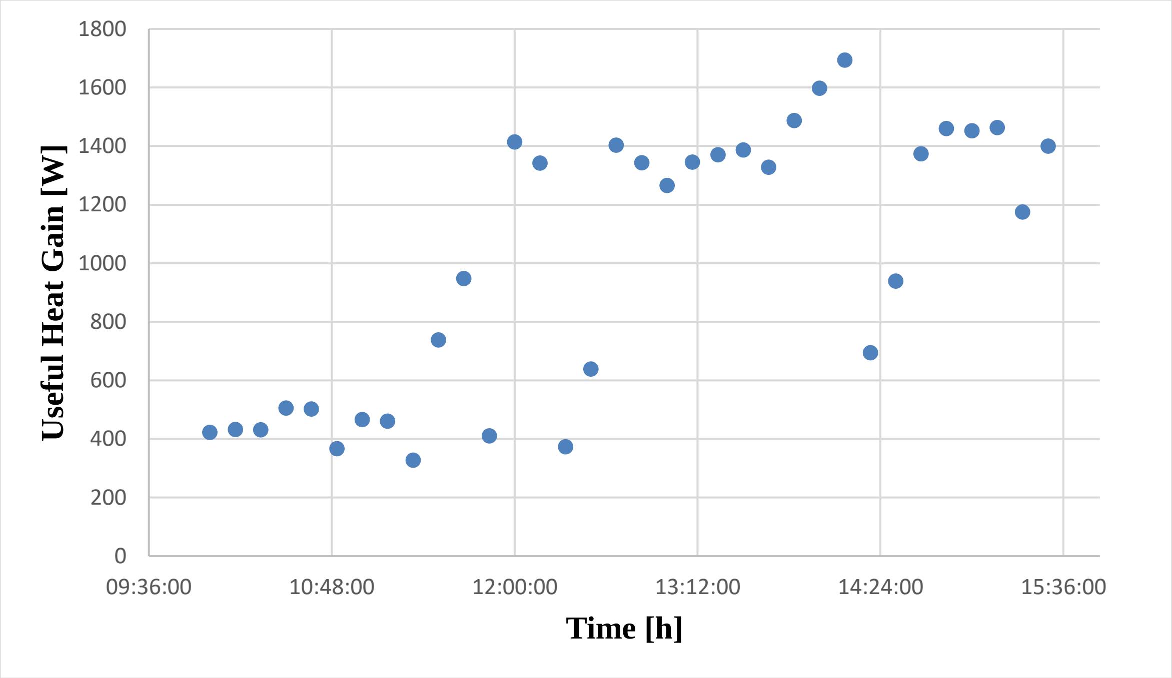

Figure 4.6. Useful heat gain.

4.5. Thermal Efficiency

The instantaneous thermal efficiency given in Figure 4.7 is calculated using the equation 2.64. A peak efficiency of 0.145 was observed at 15:30. The thermal efficiency observed is lower than expected. There are a few reasons for that:

- Errors in the tracking mechanism
- Misalignment in piping
- Bad conditions of mirrors
- Weather conditions such as high wind speed
- Dirt on the mirrors and glass cover

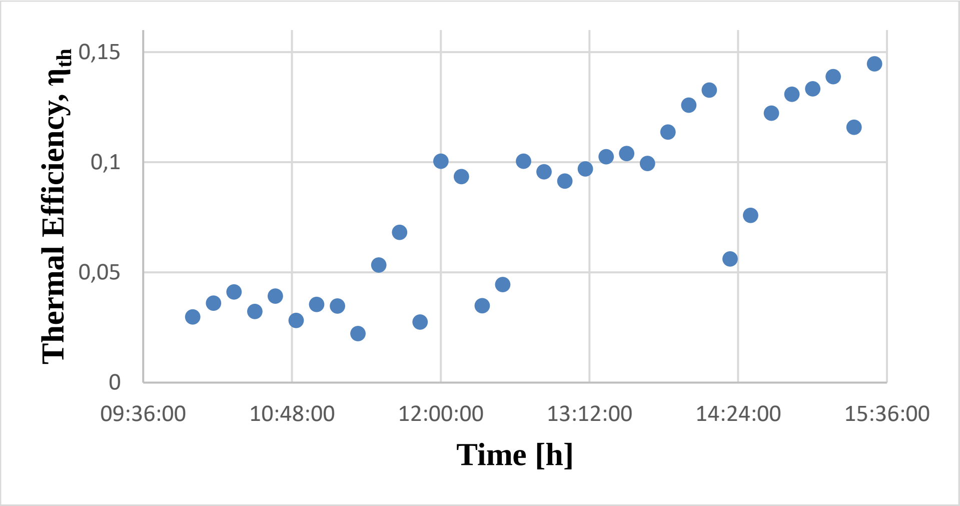

Figure 4.7. Thermal efficiency of the PTC.

Furthermore, Reynolds number is another important factor for the flow regime and thermal efficiency. The change in the Reynolds Number with time is given in Figure 4.8.

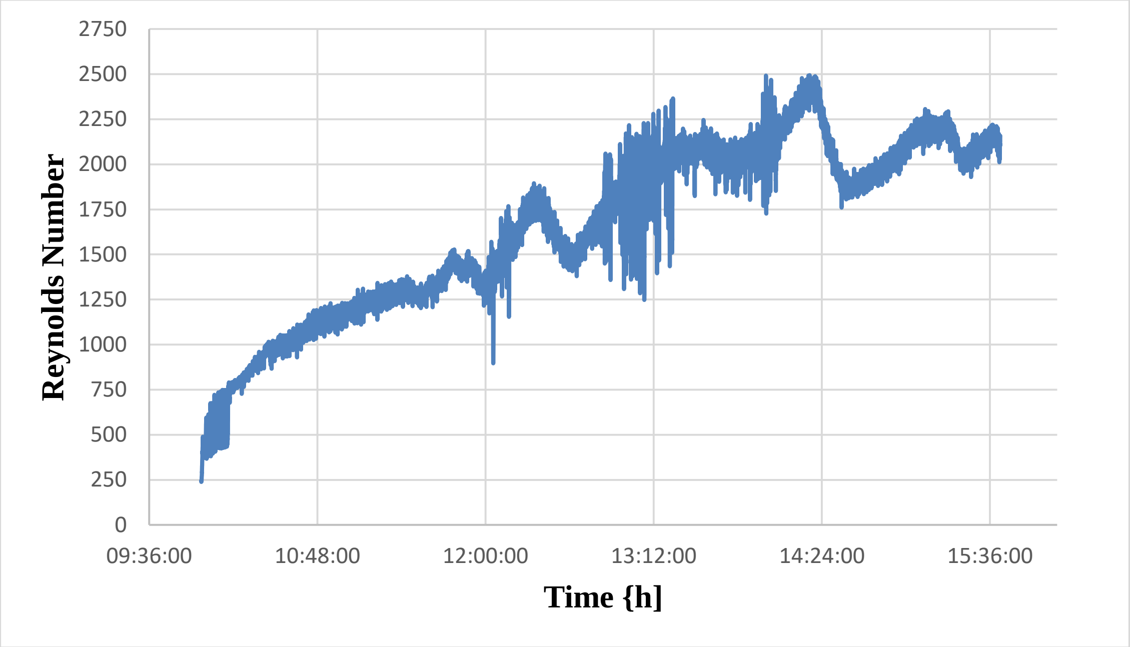

Figure 4.8. Variation of Reynolds number in the absorber tube.

When Figure 4.8 is compared with the inlet and outlet temperature graph, a resistance to temperature increase is seen between 14:10 and 14:20. At these points, the flow was in transition and the heat transfer coefficient increased dramatically as shown in Figure 4.9.

Therefore, it is reasonable that there is no temperature increase in that region for a while. Also, the peak efficiency is obtained under turbulent conditions in the absorber tube. Although there is no change in the frequency of pump and the mass flow rate, the Reynolds number increased with a decrease in the viscosity around the peak temperature of 65°C. Correlation of the Nusselt number and Reynolds number is given in Figure 4.10.

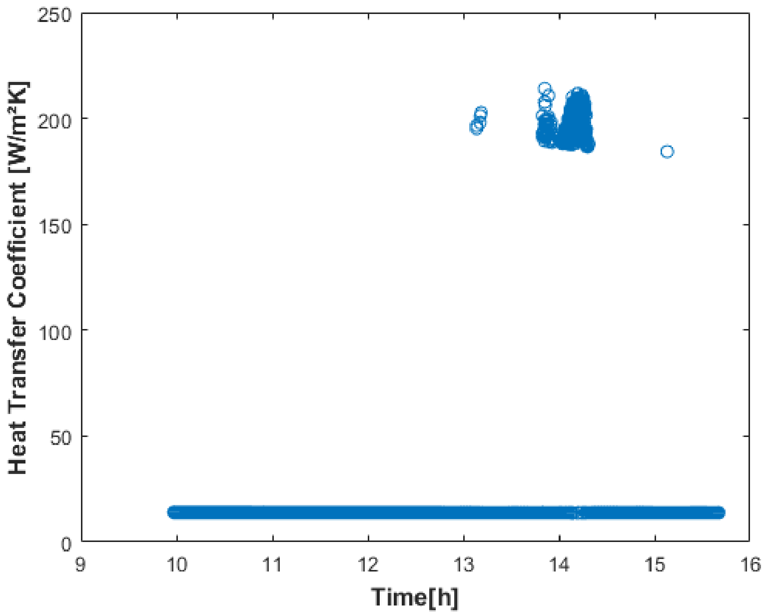

Figure 4.9. Change of heat transfer coefficient with the Reynolds number.

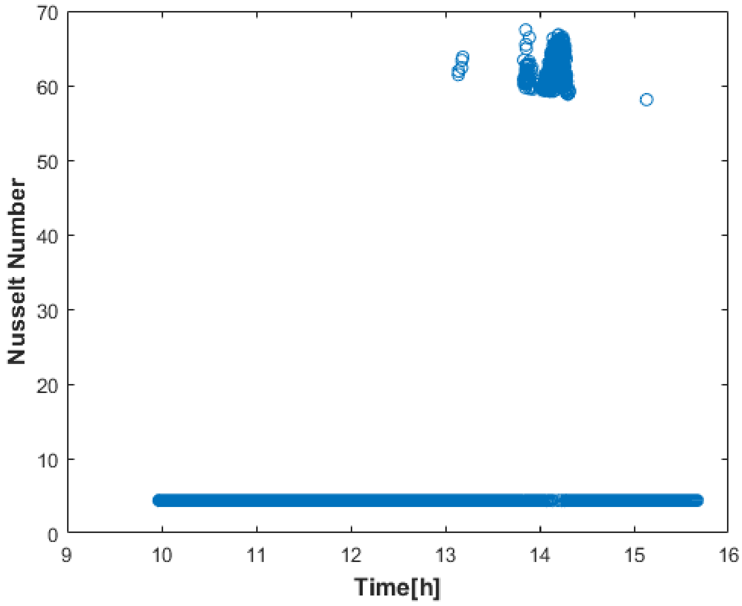

Figure 4.10. Nusselt-Reynolds numbers correlation.

4.6. Optical Efficiency

The optical efficiency depends on material properties, angle of incidence, interceptions, and geometry. It is calculated using equation 2.17. The reflectivity of mirrors, absorptivity of absorber tube, transmissivity of glass cover are crucial material properties; also, the conditions of materials using in the experiments are significant. The mirrors were in bad conditions since they stayed outside and were exposed to rain, humidity, and corrosion for the whole year. This situation highly affects the interception factor, in spite of the high reflectivity of the mirrors. Moreover, a glass of the receiver cracked around the edge during installation, which affected both optical and thermal efficiency.

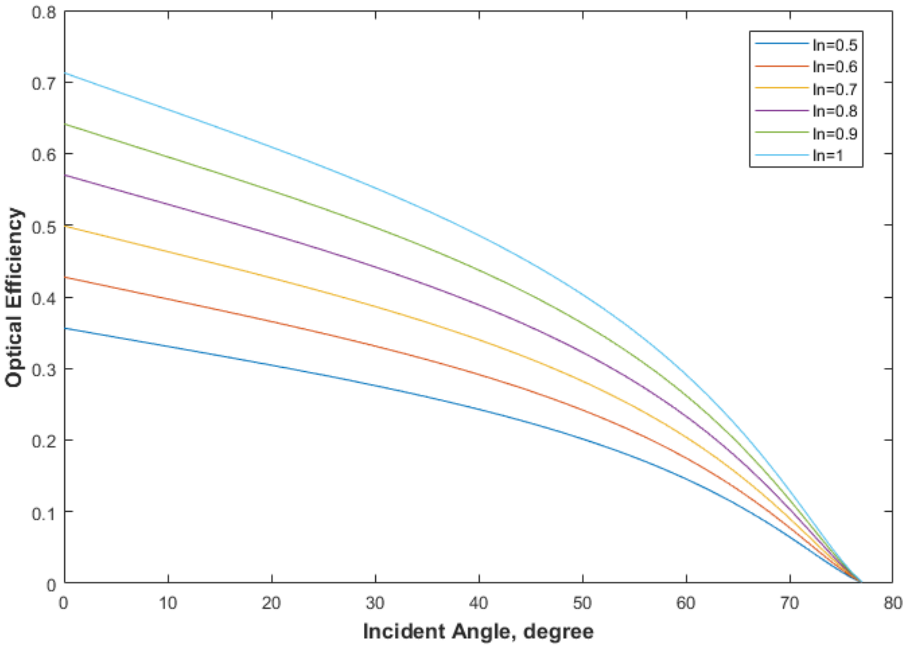

Figure 4.11. Change of the optical efficiency with the incident angle.

The angle of incidence is a crucial parameter determining the optical efficiency. Since there was a solar tracking system, the angle of incidence was assumed to be 0. It is possible to have some errors in the tracking mechanism and an increase in the angle of incidence increases. With all these parameters, the peak optical efficiency was found to be 0.7128. The change of optical efficiency with the angle of incident for different interception factors is given in Figure 4.11.

5. SUMMARY AND CONCLUSIONS

A lab scale test setup is designed for solar parabolic trough collector system with the aim of measuring inlet and outlet temperatures of collector and calculate the thermal efficiency, useful heat gain, heat loss, and optical efficiency. The test setup also enables the observation of different flow regimes such as laminar, transition and turbulent flow with the variation of the flow rate or temperature. A boiler is used as a thermal storage unit with its two coils inside. Thus, the temperature inside the boiler can be adjusted either with hot thermal oil from the collector or cold water from the chiller. A solar tracking system was implemented to the system to minimize the angle of incident and focus the sunlight on the absorber tube effectively.

The maintenance of the existing parabolic trough was carried out. The roller bearing and the shaft was renovated to place servomotor for tracking system. The cleaning of the trough and mirrors was done.; also, rusty parts in the region were rubbed with emery. The piping system was painted against corrosion with anti-aging paint. Oil was filled to the system using the corresponding valve with a circulation pump from the thermal oil tank. The air in the setup was discharged using an air relief valve before each filling process.

Several trials were performed at BURET Laboratory, on Sarıtepe Campus of Boğaziçi University in July 2019, mostly between 10:00 A.M. and 5:15 P.M on partly cloudy days. After several trials and measurements, the data for this report was collected on July 28, 2019. First of all, Experiment I was carried out between 10:00 A.M. and 3:30 P.M. The peak temperature of 65.25°C was reached at 2:20 P.M., and the peak thermal efficiency of 0.145 was obtained around 3:30 P.M. Moreover, the transition flow was observed in the receiver at around 60°C. The mass flow rate of the system was pretty steady around 65 and 70 kg/min and it is quite normal due to the decreasing viscosity. The peak of the average useful heat gain was 1694 W at 14:20, when the maximum temperature of 65.25°C was observed.

After 3:40 P.M. Experiment II was performed following the corresponding procedure. The flow was led to the coil of the boiler opening the corresponding valves and temperatures were measured. The water temperature increased up to 34.2°C at 5:10 P.M., when the HTF temperature was around 40°C. The cooling from the chiller was not required at that point.

In conclusion, expected outlet temperatures of over 100°C could not be reached in the system as calculated theoretically. If the tests are performed under clear sky conditions and with the maintenance of some parts such as mirrors, the receiver and expansion tank, which are not in ideal conditions, the optical and thermal performance of the system will increase and desired temperatures can be observed. Also, more data for turbulence conditions can be collected. With the implementation of this system, hot oil or hot water is provided for low and medium temperature applications.

5.1. Future Works

Following recommendations are suggested for future work and for improvement of the setup used:

- A compact receiver should be implemented to the system rather than a two-part receiver and the absorber tube should be painted with selective coating to increase the absorptivity,
- The expansion tank should be replaced a level above the maximum level of the receiver,
- More measurement devices such as thermocouples and pressure gauges should be implemented to the piping, especially to the inlet and outlet of boiler,
- The roller bearing and the shaft should be covered with galvanization or another method for protection against corrosion,
- The mirrors should be replaced for high optical efficiency,
- A solar sensor-based tracking system can be applied to the system for cloudy weathers,
- A check valve and a filter should be implemented to the piping,
- A numerical model for the system should be conducted to compare with the experimental data,

- Experiments should be performed at different ambient conditions, flow rates or heat transfer fluid,
- Coupling with the ORC system can be a separate study.

REFERENCES

1. Solargis, *iMaps*, https://solargis.info/imaps/, accessed in July 2019.

2. YEGM, *Güneş Enerjisi Potansiyel Atlası (GEPA)*, http://www.yegm.gov.tr/ MyCalculator/Default.aspx, accessed in July 2019.

3. NASA, *Prediction of Worldwide Energy Resource*, https://power.larc.nasa.gov/ data-access-viewer, accessed in July 2019.

4. National Renewable Energy Laboratory, *Concentrating Solar Power Projects*, https://solarpaces.nrel.gov, accessed in April 2019.

5. Vergura, S., and V. Lameira, "Technical-Financial Comparison between a PV Plant and a CSP Plant", *SSRN*, Vol. 6, pp. 210–220, 2012.

6. Chu, Y., "Review and Comparison of Different Solar Energy Technologies, Annual Report", *Global Energy Network Institute*, California, 2011.

7. Ju, X., C. Xu, Y. Hu, X. Han, G. Wei, and X. Du, "A review on the development of photovoltaic/concentrated solar power (PV-CSP) hybrid systems," *Solar Energy Materials and Solar Cells*, Vol. 161, pp. 305-327, 2017.

8. REN21 Secretariat, *Renewables 2017 Global Status Report*, https://www.wame2015.org/files/catalogue/2018/6/17_8399_GSR_2017_Full_Report_0621_Opt_1.pdf, accessed in May 2019.

9. International Renewable Energy Agency, *Renewable Energy Capacity Statistics*, https://www.irena.org/-/media/Files/IRENA/Agency/Publication/2019/Mar/IRENA_RE_Capacity_Statistics_2019.pdf, accessed in May 2019.

10. Kalogirou, S. A., *Solar Energy Engineering: Processes and Systems: Second Edition*, Academic Press, 2014.

11. IEA-ETSAP & IRENA, “Concentrating Solar Power Technology Brief”, 2013.

12. IEA, *Is concentrating solar power forecast to contribute to global energy storage?*, https://www.iea.org/newsroom/news/2019/march/is-concentrating-solar-power-forecast-to-contribute-to-global-energy-storage.html, accessed in May 2019.

13. Paul, W., *Collinsville solar-gas hybrid project: meeting the climate change challenge by combing proven technologies in a new way and reusing existing infrastructure*, https://williampaulbell.wordpress.com/2014/11/26/collinsville-solar-gas-hybridproject-meeting-the-climate-change-challenge-by-combing-proven-technologies-in-a new-way-and-reusing-existing-infrastructure, accessed in May 2019.

14. PennState, *Parabolic Dish CSP Technology EME 812: Utility Solar Power and Concentration*, https://www.e-education.psu.edu/eme812/node/648, accessed in May 2019.

15. Parabolic Trough Power Plant, *Concentrated Solar Power: Parabolic Trough Power Plant*, https://www.mtholyoke.edu/~wang30y/csp/PTPP.html#_edn1, accessed in April 2019.

16. Alternative Energy Tutorials, *Parabolic Trough Reflector for Solar Thermal System*, http://www.alternative-energy-tutorials.com/solar-hot-water/parabolic-trough-reflector.html, accessed in May 2019.

17. Uckun, C., *Modeling and simulations of direct steam generation in concentrating solar power plants using parabolic trough collectors*, M.S Thesis, Middle East Technical University, 2013.

18. Alguacil, M., C. Prieto, A. Rodriguez, and J. Lohr, “Direct steam generation in parabolic trough collectors”, in *Energy Procedia*, Vol. 49, pp. 21-29, 2013.

19. Kalogirou, S. A., *Solar Energy Engineering: Processes and Systems*, Academic Press, 2009.

20. Günther, M., M. Joemann, and S. Csambor, “Advanced CSP Teaching Materials Chapter 5 Parabolic Trough Technology,” *Advanced CSP Teaching Materials*, Enermena, Germany, 2011.

21. Ragheb, M., “Solar Thermal Power and Energy Storage Historical Perspective”, 2014.

22. Winter, C. J., R. L. Sizmann, and L. L. Vant-Hull, *Solar Power Plants : Fundamentals, Technology, Systems, Economics*. Springer Berlin Heidelberg, 1991.

23. Solar Millenium, *The parabolic trough power plants Andasol 1 to 3*, Erlangen, 2008.

24. Chafie, M., M. F. Ben Aissa, S. Bouadila, M. Balghouthi, A. Farhat, and A. Guizani, “Experimental investigation of parabolic trough collector system under Tunisian climate: Design, manufacturing and performance assessment”, *Applied Thermal Engineering*, Vol. 11, No.741, 2016.

25. Rehan, M. A., M. Ali, N. A. Sheikh, M. S. Khalil, G. Q. Chaudharry, “Experimental performance analysis of low concentration ratio solar parabolic trough collectors with nanofluids in winter conditions”, *Renewable. Energy*, Vol. 118, pp. 742-751, 2018.

26. Potenza, M., M. Milanese, G. Colangelo, and A. de Risi, “Experimental investigation of transparent parabolic trough collector based on gas-phase nanofluid”, *Applied Energy*, Vol. 203, pp. 560-570, 2017.

27. Qu, W., R. Wang, H. Hong, J. Sun, and H. Jin, “Test of a solar parabolic trough collector with rotatable axis tracking”, *Applied Energy*, Vol. 207, pp. 7-17, 2017.

28. Al Asfar, J., O. Ayadi, and A. Al Salaymeh, “Design and performance assessment of a parabolic trough collector”, *Jordan Journal of Mechanical and Industrial Engineering*, Vol. 8, No.1, pp. 1-5, 2014.

29. Filho, V. C. P., A. B. De Sá, J. C. Passos, and S. Colle, “Experimental and numerical analysis of thermal losses of a parabolic trough solar collector”, in *Energy Procedia*, Vol. 57, pp. 381-390, 2014.

30. Jamal-Abad, M. T., S. Saedodin, and M. Aminy, “Experimental investigation on a solar parabolic trough collector for absorber tube filled with porous media”, *Renewable Energy*, Vol. 107, pp. 156-163, 2017.

31. “Methods of testing to determine the thermal performance of solar collectors”, *ASHRAE Standards*, 2003.

32. Coccia, G., G. Di Nicola, and M. Sotte, “Design, manufacture, and test of a prototype for a parabolic trough collector for industrial process heat”, *Renewable Energy*, Vol. 74, pp. 727-736, 2014.

33. Zou, B., J. Dong, Y. Yao, and Y. Jiang, “An experimental investigation on a small-sized parabolic trough solar collector for water heating in cold areas”, *Applied Energy*, Vol. 163, pp. 396-407, 2016.

34. Qu, H. and M. Wang, “Experimental Study of a Parabolic Trough Medium Temperature Solar Thermal System”, *International Conference on Solar Heating and Cooling for Buildings and Industry, Energy Procedia*, Vol. 70, pp. 504-509, 2015.

35. Lei, D., Q. Li, Z. Wang, J. Li, and J. Li, “An experimental study of thermal characterization of parabolic trough receivers”, *Energy Conversion and Managament*, Vol. 69, pp. 107-115, 2013.

36. Sivaram, P. M., N. Nallusamy, and M. Suresh, “Experimental and numerical investigation on solar parabolic trough collector integrated with thermal energy storage unit”, *International Journal of Energy Research*, Vol. 40, pp. 1564-1575, 2016.

37. Bortolato, M., S. Dugaria, and D. Del Col, “Experimental study of a parabolic trough solar collector with flat bar-and-plate absorber during direct steam generation”, *Energy*, Vol. 116, pp. 1039-1050, 2016.

38. Lu, J. F., J. Ding, J. P. Yang, and K. Wang, “Heat Loss Measurement and Analyses of Solar Parabolic Trough Receiver”, *Applied Mechanics and Materials*, Vol. 291-294, pp. 127-131, 2013.

39. Kumaresan, G., P. Sudhakar, R. Santosh, and R. Velraj, “Experimental and numerical studies of thermal performance enhancement in the receiver part of solar parabolic trough collectors”, *Renewable and Sustainable Energy Reviews*, Vol. 77, pp. 1363-1374, 2017.

40. Soysal, U., *Analysis and Optimization of a Small Scale Solar Organic Rankine Cycle System for Power Generation*, M.S Thesis, Boğaziçi University, 2017.

41. Çağlar, A., “Design of a Parabolic Trough Solar Collector Using a Concentrator with High Reflectivity”, *Proceedings of the 2nd World Congress on Mechanical, Chemical, and Material Engineering*, 2016.

42. Murtuza, S. A., H. V. Byregowda, M. M. A. H, and M. Imran, “Experimental and simulation studies of parabolic trough collector design for obtaining solar energy”, *Resource Efficient Technologies*, Vol. 3, pp. 414-421, 2017.

43. Kumar, S. and D. Kumar, “Thermal performance of the solar parabolic trough collector at different flow rates: an experimental study”, *International Journal of Ambient Energy*, pp. 93-102, 2018.

44. Günther, M., “Advanced CSP Teaching Materials Chapter 2: Solar Radiation”, *Advanced CSP Teaching Materials*, Enermena, Germany, 2011.

45. Goswami, F., *Principles of Solar Engineering*, Third Edition. Philadelphia, PA.: Taylor & Francis, 2000.

46. Padilla, R. V., E. Stefanakos, M. M. Rahman, J. T. Wolan, and Y. You, *Simplified Methodology for Designing Parabolic Trough Solar Power Plants*, Ph.D Thesis, University of South Florida, 2011.

47. Maleki, S. A., M. H. Hizam, and C. Gomes, “Estimation of hourly, daily and monthly global solar radiation on inclined surfaces: Models re-visited”, *Energies*, Vol. 10, pp. 134-162, 2017.

48. Bellos, E. and C. Tzivanidis, “Alternative designs of parabolic trough solar collectors”, *Progress in Energy and Combustion Science*, Vol. 71, pp. 81-117, 2019.

49. Coccia, G., G. Di Nicola, and A. Hidalgo, *Parabolic Trough Collector Prototypes for Low-Temperature Process Heat*, Springer Briefs in Applied Science Technology, 2016.

50. Gaul, H. and A. Rabl, “Incidence-Angle Modifier and Average Optical Efficiency of Parabolic Trough Collectors”, *Journal of Solar Energy Engineering*, pp. 16-21, 2010.

51. Mutlak, F. A. A, *Design and fabrication of parabolic trough solar collector for thermal energy applications*, Ph.D Thesis, University of Baghdad, 2011.

52. Tzivanidis, C., E. Bellos, D. Korres, K. A. Antonopoulos, and G. Mitsopoulos, “Thermal and optical efficiency investigation of a parabolic trough collector”, *Case Studies in Thermal Engineering*, Vol. 6, pp. 226-237, 2015.

53. Forristall, R., *Heat Transfer Analysis and Modeling of a Parabolic Trough Solar Receiver Implemented in Engineering Equation Solver*, Technical Report, National Renewable Energy Laboratory, 2003.

54. Gnielinski, V., “New equations for heat and mass transfer in turbulent pipe and channel flow”, *International Chemical Engineering*, Vol. 16, No. 2, pp.359-368, 1976.

55. Colebrook, C. F., “Turbulent Flow in Pipes, with particular reference to the Transition Region between the Smooth and Rough Pipe Laws”, *Journal of Institution of Civil Engineers*, Vol. 11, No. 4, pp. 133-156, 1939.

56. Ratzel, A. C., C. E. Hickox, and D. K. Gartling, “Techniques for Reducing Thermal Conduction and Natural Convection Heat Losses in Annular Receiver Geometries”, *Journal of Heat Transfer*, Vol. 101, No. 1, pp. 108-113, 1979.

57. Martin, M. and P. Berdahl, “Characteristics of infrared sky radiation in the United States”, *Solar Energy*, Vol. 33, pp. 321-336, 1984.

58. Brooks, M. J., I. Mills, and T.M. Harms “Perfomance of a Parabolic Trough Solar Collector”, *Journal of Southern Energy in Southern Africa*, Vol. 17, No. 3, 2006.

59. SCHOTT, *Brochure of DURAN*, https://www.schott.com/d/tubing/66ee849c-cad9-42a3-97cb-67fd0534e3fb/schott_duran_brochure_gb_final.pdf, accessed in June 2019.

60. FUCHS, *Product Information: Renolin Therm 320*, http://www.fareastfish.ru/upload/iblock/9a3/9a3f7d1f693d0398acab40d390c8008a.pdf, accessed in June 2019.

61. Elimko, *Straight Type Thermocouples*, http://www.elimko.com.tr/files/D%C3%BCzTipTermokupllar.pdf, accessed in June 2019.

62. PAKKENS, *PAKKENS Dial Thermometers*, https://www.pakkens.com/en/product/te-100-171, accessed in June 2019.

63. ABB, *Data Sheet of Vortex Master FSV430, and FSV450* https://library.e.abb.com/public/664951bec61c4f9092cb23cb6484376b/DS_FSV430_450_EN_F.pdf, accessed in June 2019.

64. E+E ELEKTRONIK, *High-Precision Air and Gas Velocity Transmitter for Industrial Applications*, https://www.instrumart.com/assets/EplusE-EE75-Datasheet.pdf, accessed in July 2019.

65. BURES, *Meteorology Data of Sarıtepe Campus*, 2018.